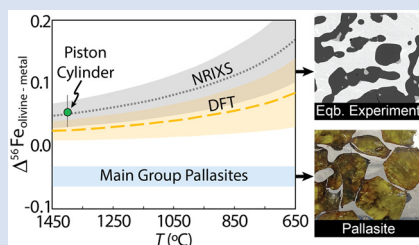# Iron isotope evidence of an impact origin for main-group pallasites

N.R. Bennett[1,2,3*†], C.K. Sio[1,2,4*†], E. Schauble[5], C.E. Lesher[3,6], J. Wimpenny[4], A. Shahar[2]

OPEN ACCESS

Abstract

https://doi.org/10.7185/geochemlet.2229

Despite decades of work, the origin of pallasite meteorites has remained enigmatic. Long thought to be samples of the core-mantle boundary of differentiated asteroids, more recent studies have suggested a range of mechanisms for pallasite formation. These include olivine-metal mixing during a planetesimal collision and the intrusion of over-pressured core liquids into a planetesimal mantle. Establishing if the olivine and metal that comprise pallasites were once equilibrated at high temperature remains key to discriminating between these hypotheses. To this end, we determined the iron isotope compositions of olivine and metal in eleven main-group pallasites and found, in all cases, that olivine is isotopically lighter than metal. To interpret these data, we constrained the olivine-metal equilibrium Fe isotope fractionation with *ab initio* calculations and high temperature experiments. These independent approaches show that olivine preferentially incorporates the heavy isotopes of iron relative to metal. Our results demonstrate that pallasitic olivine and metal never achieved isotopic equilibrium with respect to iron. This precludes extended cooling at high temperature and is best reconciled with an impact origin for the main-group pallasites.

Introduction

Pallasites are predominately composed of Fe-Ni metal and olivine. Traditionally, they are interpreted to be remnants of core-mantle boundary material from differentiated asteroids, an idea which continues to merit discussion (*e.g.,* McKibbin *et al., 2019*). Alternatively, pallasites may form in the shallow mantle of an asteroid either by ferrovolcanism (Johnson *et al., 2020*), impact-induced local heating and igneous differentiation (Mittlefehldt, 1980), or injection of exogeneous metal into the mantle of the pallasite parent body (Tarduno *et al., 2012*). One way to distinguish these varied formation mechanisms is by constraining the thermal history of pallasites. A core-mantle boundary origin suggests a protracted period of cooling at high temperature, during which elemental and isotopic equilibrium between phases would be achieved. In contrast, a shallow mantle or impact mixing origin may be accompanied by more rapid cooling from high temperature, thus limiting re-equilibration. The low temperature thermal history of pallasite meteorites is well constrained by metallographically determined cooling rates, however, there remains little information on their high temperature thermal history. Here, we constrain this high temperature history by combining 1) Fe isotope measurements of main-group pallasites (MGP), 2) the equilibrium olivine-metal Fe isotope fractionation determined from high temperature experiments and *ab initio* calculations, and 3) models of planetesimal cooling and olivine-metal equilibration.

Several studies have attempted to determine equilibration temperatures for pallasites from the apparent partitioning of elements between olivine and metal (*e.g.,* Seifert *et al., 1988*). However, these studies assume equilibrium rather than test for it. Iron stable isotope data measured in olivine and metal have also been evaluated previously for geothermometry, but the results are highly variable (Poitrasson *et al., 2005*; Weyer *et al.,* 2005; Chernonozhkin *et al., 2016*). These large variations result from unrepresentative sampling of the metal, which is composed of taenite (face-centred cubic or fcc Fe-Ni) and kamacite (body-centred cubic or bcc Fe-Ni) that form Widmanstätten patterns. At high temperature, Fe-Ni alloy is present with an fcc crystal structure (Yang *et al., 2010*). As temperature decreases, this phase unmixes into coexisting Fe-rich and Fe-poor metallic phases; kamacite and taenite, respectively. Kamacite growth is diffusion-limited by the supply of iron from taenite (Dauphas, 2007). As the light isotopes of iron diffuse faster, kamacite is slightly enriched in light isotopes while heavy isotopes concentrate in taenite. Iron diffusion in taenite is 3 orders of magnitude slower than in kamacite. Taenite therefore retains significant gradients in isotope composition. As a result, preferential sampling of taenite will displace the Fe isotope composition to heavy values. In contrast, kamacite contains the bulk (>85 %) of the metallic Fe in pallasites and diffusion within kamacite is sufficiently rapid to homogenise Fe isotopes (Dauphas, 2007). The result is that kamacite closely approximates the bulk metal isotopic composition. Accordingly, we sampled kamacite to

1. University of Toronto, Department of Earth Sciences, 22 Ursula Franklin St, Toronto, ON M5S 3B1, Canada
2. Geophysical Laboratory, Carnegie Institution for Science, 5251 Broad Branch Rd NW, Washington, DC 20015, USA
3. Department of Earth and Planetary Sciences, University of California, Davis, CA 95616, USA
4. Lawrence Livermore National Laboratory, 7000 East Ave, Livermore, CA 94550, USA
5. Department of Earth, Planetary, and Space Sciences, University of California, Los Angeles, CA 90095, USA
6. Department of Geoscience Science, Aarhus University, Aarhus, 8200, Denmark
* Corresponding author (email: neil.bennett@utoronto.ca; corliss.sio@utoronto.ca)
† These authors contributed equally to this work.

obtain a representative measurement of the bulk metal Fe isotope compositions of pallasite meteorites.

Sound interpretation of this Fe isotope data relies on access to a robust olivine-metal fractionation factor. However, the direction of fractionation is debated (Polyakov and Mineev, 2000; Dauphas et al., 2014), complicating the interpretation of data collected on natural samples. To resolve this issue, we employed multiple techniques to determine Fe isotope fractionation between olivine and metal. As different metal phases are present in the pallasites, it is imperative to determine which phase could have equilibrated with olivine. Although the metal phase presently in contact with olivine is kamacite (bcc-Fe), olivine-metal isotopic equilibrium could not have been achieved in the stability field of kamacite. For the mean Ni contents of MGP metal (10.6 wt. % Ni; Wasson and Choi, 2003), kamacite formation begins at ~650 °C. For an average pallasite cooling rate of 7 °C/Myr (Yang et al., 2010) and a median olivine diameter of 4 mm (Wasson and Choi, 2003), the closure temperature for iron in olivine is also ~650 °C (see Supplementary Information). Accordingly, if there were any chance of equilibration between olivine and metal it would have occurred when olivine was in contact with a single fcc-metal phase or metallic liquid (i.e. at higher temperatures). Therefore, our ab initio calculations and equilibration experiments focused on fcc-Fe and liquid metal phases.

Results and Discussion

Eleven MGP were analysed by micro-drilling kamacite and adjacent olivine crystals (Fig. S-1). To illustrate the range of data that can be obtained by untargeted sampling, metal and olivine were also handpicked and processed. All samples were analysed for their Fe isotope compositions by multi-collector inductively coupled plasma mass spectrometry (MC-ICPMS). Iron isotope compositions are reported in δ notation:

$$\delta^{56}Fe_{smp}(‰) = 1000 \times \left(\frac{^{56}Fe/^{54}Fe_{smp}}{^{56}Fe/^{54}Fe_{std}} - 1 \right) \qquad \text{Eq. 1}$$

where smp denotes the sample (i.e. bulk metal, olivine) and std denotes the Fe isotopic standard IRMM-524a. Isotopic fractionations are expressed in Δ notation:

$$\Delta^{56}Fe_{olivine-metal} = \delta^{56}Fe_{olivine} - \delta^{56}Fe_{metal} \qquad \text{Eq. 2}$$

In all eleven MGP, the olivine fractions are consistently lighter than the metal fractions (Fig. 1). The range of measured isotope fractionation is reduced by a factor of ~3 compared to literature data (Fig. S-2). Data for our handpicked samples reproduced the range of $\Delta^{56}Fe_{olivine-metal}$ obtained in previous studies, showing that the variability in $\Delta^{56}Fe_{olivine-metal}$ reported in previous studies reflects biased sampling of the metal fractions. Based on the rationale that all MGP come from the same parent body (Greenwood et al., 2015), we report the weighted average $\Delta^{56}Fe_{olivine-metal}$ of −0.049 ‰ ± 0.016 ‰.

Using density functional theory (DFT), we calculated force constants for the iron sublattices in olivine (159 ± 10 N/m) and fcc-metal (134 ± 6 N/m). Due to difficulty in modelling the magnetic structure of taenite, the fcc-metal modelled here is awaruite ($FeNi_3$). To evaluate the effect of Ni on the force constant for Fe in fcc-metal, tetrataenite (FeNi), which has an fcc-like structure (Clarke and Scott, 1980), was also modelled. The force constant for tetrataenite is 142 ± 6 N/m, which is slightly higher but identical within error to awaruite, suggesting that Ni has no significant effect on the force constant of iron in fcc-metal. As olivine has a larger force constant, $\Delta^{56}Fe_{olivine-metal}$ is always positive.
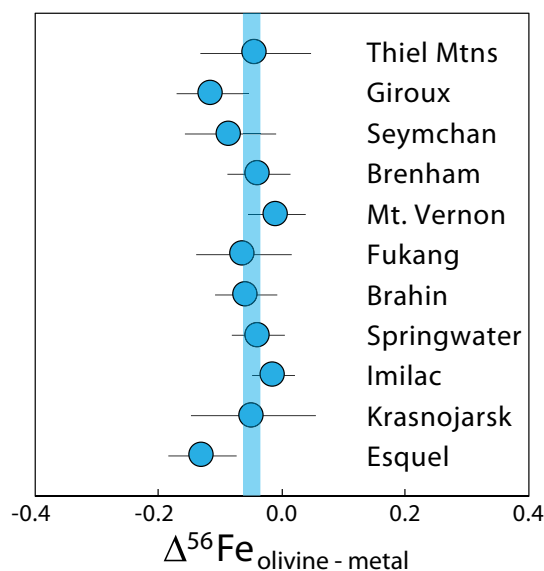

Figure 1 Measured Fe isotope fractionations between olivine and bulk metal in MGP. The blue band shows the weighted average for the 11 MGP measured in this study, plotted in order of cooling rate (Esquel slowest, Giroux fastest and Thiel Mtns. unknown; Yang et al., 2010).

To provide another independent constraint on $\Delta^{56}Fe_{olivine-metal}$, we performed piston cylinder experiments that directly equilibrate olivine and Fe ± Ni metal at high temperature. Olivine-metal assemblages were enclosed in graphite capsules, pressurised to 1 GPa, then heated to 1400 °C for 3.5–95 hr before quenching. These conditions are similar to those estimated for the core-mantle boundary of the pallasite parent body (1330 °C; Wasson and Choi, 2003, and ~0.1 GPa). Although our experimental pressure is higher than estimated for pallasites, Clayton et al. (1975) showed that between 0.1 and 2.0 GPa, pressure has no effect on equilibrium isotope fractionation factors. The bonding environment for molten metal in these experiments is similar to that of fcc-metal (see Supplementary Information). As with our DFT calculations, we did not observe an effect of Ni on the olivine-metal Fe isotope fractionation. The weighted average of three equilibrated experiments yields $\Delta^{56}Fe_{olivine-metal} = +0.054 ± 0.027‰$ at 1400 °C. This value is in excellent agreement with our DFT calculations, as well as the prediction made using nuclear resonant inelastic X-ray scattering data (NRIXS; Dauphas et al., 2014; Krawczynski et al., 2014).

To our knowledge, this is the first time that a single Fe isotope fractionation factor has been corroborated using all three of these independent approaches. We are thus confident that at conditions relevant to asteroidal core formation, heavy Fe isotopes preferentially partition into olivine relative to metal at equilibrium. The data obtained for MGP, however, show the opposite sense of fractionation (Fig. 2), suggesting that coexisting olivine and metal in pallasites never achieved Fe isotope equilibrium. Kinetic and equilibrium processes occurring at low temperature may potentially overprint high temperature equilibrium isotopic signatures. These processes, however, cannot reverse the direction of olivine-metal Fe isotope fractionation (see Supplementary Information).

Having established that olivine and metal are not in Fe isotope equilibrium, it is possible to determine parent body conditions where olivine-metal annealing could have taken place without leading to isotopic equilibrium. We coupled a 1 D
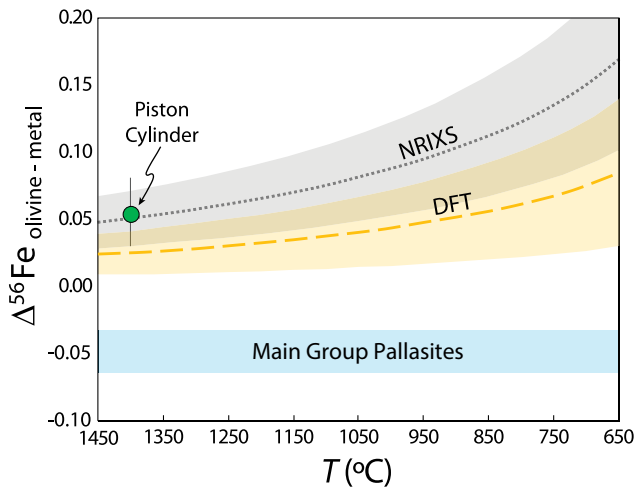
Figure 2 Grey and yellow bands show predicted olivine-metal Fe isotope fractionations at equilibrium, based on NRIXS and our DFT calculations, respectively. The piston cylinder datum is the weighted average of three isotopically equilibrated laboratory experiments. All methods show the same direction of equilibrium olivine-metal fractionation. MGP display the opposite sense of fractionation, suggesting that MGP olivine and metal are not in Fe isotopic equilibrium.

temperatures remain too high to prevent isotopic equilibrium. This result persists for a wide range of core diameters and mantle thicknesses (Fig. 3b). Our modelling therefore demonstrates that a core-mantle boundary, or other deep mantle, origin for pallasites is not compatible with the observed Fe isotope disequilibrium.

We next turn our attention to pallasite formation models that allow for a shallow to mid-mantle origin for MGP: 1) ferrovolcanism (Fig. 4a; Johnson et al., 2020), and 2) impact-induced mixing of olivine and metal on the MGP parent body, involving either an endogenous (e.g., Mittlefehldt, 1980) or exogenous (e.g., Kruijer et al., 2022; Windmill et al., 2022) source of metal (Fig. 4b,c).

Johnson et al. (2020) proposed that pallasites form when evolved, over-pressured, core liquids intrude the overlying mantle and entrain olivine in the process. The required over-pressure is facilitated by light element enriched (i.e. more buoyant) core liquid compositions. Light element (namely S) enrichment of planetesimal core liquids is achieved via fractional crystallisation. Ni et al. (2020) demonstrated that fractional crystallisation of Fe-S alloys is accompanied by enrichment of the S-rich liquid in light Fe isotopes. The heavy Fe isotope compositions of the bulk metals measured in this study (Fig. S-2) are not indicative of an evolved S-rich liquid, and thus do not lend support for the ferrovolcanism model.

An alternative is impact-induced mixing of endogenous olivine and metal reservoirs without complete parent body disruption. An impact into a cold body can raise the local temperature sufficiently to facilitate melting if the bodies have high porosities (Davison et al., 2012). Partial melting of a chondritic composition requires high temperatures (> 1100 °C; Jurewicz et al., 1993), that must be sustained long enough to permit igneous differentiation into discrete metal and silicate (olivine) reservoirs that are not isotopically equilibrated with each other. These reservoirs must then be mixed and cooled quickly enough to prevent isotopic re-equilibration. The plausibility of this
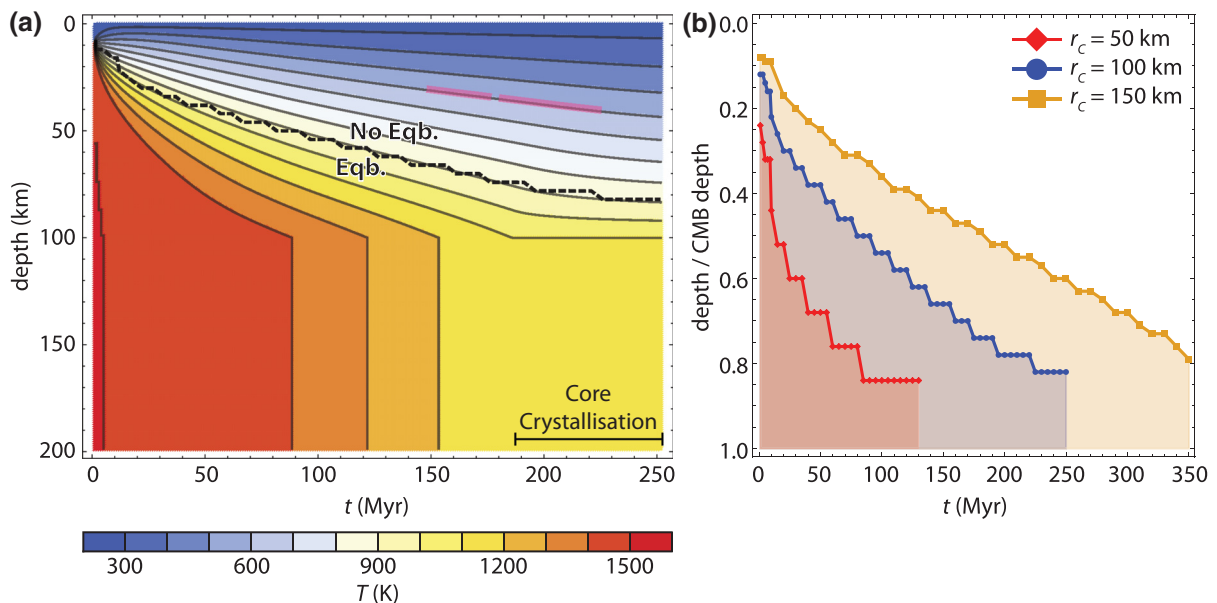
planetesimal cooling model with simultaneous diffusive Fe exchange between olivine and metal to place constraints on the depth and timing of olivine-metal mixing in the MGP parent body (see Supplementary Information). Figure 3a displays the results of one of these models, which was performed at conditions that also satisfy previous palaeomagnetic constraints on MGP. The black dashed curve marks the depth and timing of olivine-metal mixing above which Fe isotopic disequilibrium would be maintained. The key takeaway from this model is that even for late-stage olivine-metal mixing, core-mantle boundary

Figure 3 (a) Cooling and olivine-metal mass exchange model for a 200 km radius body with the core mantle boundary located at 100 km depth. The black dashed curve shows the time and depth of olivine-metal mixing above which Fe isotope equilibrium is inhibited. MGP formed above this curve. Also shown are the emplacement depths and periods of cloudy zone formation for the Imilac and Esquel meteorites, determined following Bryson et al. (2015). (b) Equilibrium curves for the same planetary radius but with different core radii (r_C). The shaded regions indicate where olivine-metal equilibrium will occur for each model. Regardless of core size, olivine and metal always equilibrate when mixed near the core-mantle boundary. Note that in all cases models are terminated once the core is fully crystallised.
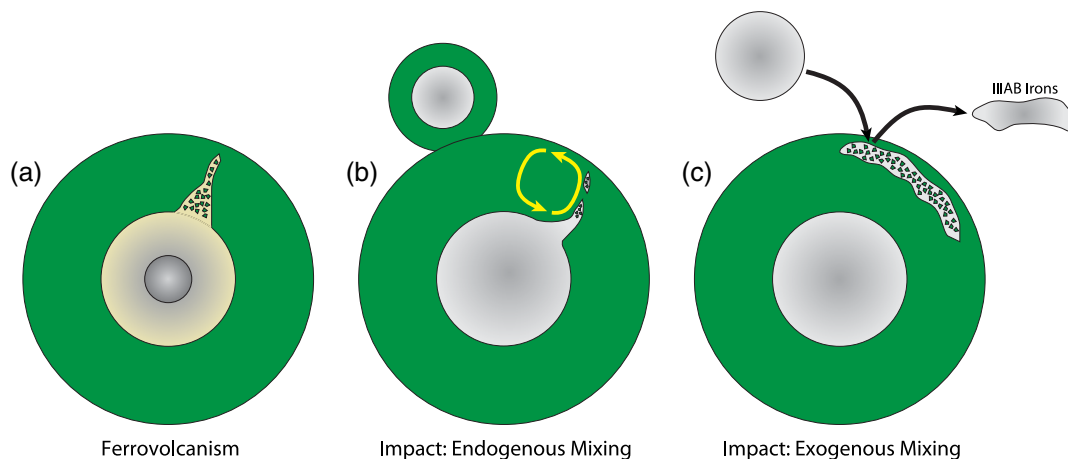
Figure 4 MGP formation models that account for shallow depths of olivine-metal mixing. Our Fe isotope data are most readily explained by model (c).

scenario is difficult to assess, particularly given our limited knowledge of the mineral-melt Fe isotope fractionation factors that control igneous differentiation. Measurements of O isotopes in pallasites, however, suggest that olivine and metal were sourced from different planetesimal bodies, precluding such an endogenous origin (Windmill *et al.*, 2022).

Kruijer *et al.* (2022) provided W and Mo isotopic evidence that the metal from MGP is genetically related to the IIIAB irons, verifying an idea that originated from the trace element compositions of these meteorite groups (Scott, 1977). Furthermore, Yang *et al.* (2010) showed that IIIAB irons cooled significantly faster than MGP. These observations can be explained if the IIIAB core collided with the MGP parent body in a hit-and-run collision, leading to the rapid cooling of run-away metal that was exposed to space (Fig. 4c). This scenario also accommodates olivine-metal mixing in the shallow to mid-mantle of the MGP parent body, where Fe isotope equilibration between these phases is inhibited. Emplacement at these depths also permits MGP metal to cool below its blocking temperature before complete solidification of the parent body core and concomitant extinction of the dynamo (Tarduno *et al.*, 2012; Bryson *et al.*, 2015; Nichols *et al.*, 2021).

The subsequent slow cooling phase, as required by MGP metallographic cooling rates (3–18 °C/Myr; Yang *et al.,* 2010), must begin at a temperature below ~650 °C – low enough to inhibit iron diffusion in olivine, but high enough for Widmanstätten patterns to develop. While this two stage cooling history for MGP has previously been suggested on the basis of deformation experiments (Walte *et al.*, 2020), our study provides the corroborating geochemical evidence needed to cement this hypothesis and an impact origin for MGP.

Conclusion

There now exists multiple lines of evidence that MGP did not form near a core-mantle boundary: 1) The genetic link between IIIAB irons and MGP metals, and their difference in cooling rates, can only be explained by the impact of the IIIAB core into the MGP parent body, 2) palaeomagnetic data requires MGP metal crystallisation during an extant core dynamo, and 3) the Fe isotope data presented here demonstrate that olivine and metal are not in isotopic equilibrium, requiring rapid cooling to the olivine closure temperature. Our iron isotope measurements on pallasites, coupled with new constraints on the olivine-metal fractionation factor, demonstrate that pallasites

originated from shallow to mid-mantle depths in the parent body. Our findings support a growing consensus that main-group pallasites formed *via* an impact that provided an exogenous source of metal.

Author Contributions

NRB, CKS, and AS conceived the study. NRB performed the piston cylinder experiments, electron microprobe analyses, and coupled thermal and diffusion modelling. CKS performed the ICPMS and MC-ICPMS analyses and guided the diffusion calculations. ES performed the DFT calculations and wrote the relevant methods section. NRB and CKS wrote the manuscript with input from all co-authors.

Acknowledgements

Editor: Helen Williams

Additional Information

Supplementary Information accompanies this letter at https://www.geochemicalperspectivesletters.org/article2229.

References

Bryson, J.F., Nichols, C.I., Herrero-Albillos, J., Kronast, F., Kasama, T., Alimadadi, H., van der Laan, G. Nimmo, F., Harrison, R.J. (2015) Long-lived magnetism from solidification-driven convection on the pallasite parent body. *Nature* 517, 472–475. https://doi.org/10.1038/nature14114

Chernonozhkin, S.M., Goderis, S., Costas-Rodríguez, M., Claeys, P., Vanhaecke, F. (2016) Effect of parent body evolution on equilibrium and kinetic isotope fractionation: a combined Ni and Fe isotope study of iron and stony-iron meteorites. *Geochimica et Cosmochimica Acta*, 186, 168–188. https://doi.org/10.1016/j.gca.2016.04.050

Clarke, R.S., Scott, E.R. (1980) Tetrataenite—ordered FeNi, a new mineral in meteorites. *American Mineralogist* 65, 624–630.

Clayton, R.N., Goldsmith, J.R., Karel, K.J., Mayeda, T.K. (1975). Limits on the effect of pressure on isotopic fractionation. *Geochimica et Cosmochimica Acta* 39, 1197–1201. https://doi.org/10.1016/0016-7037(75)90062-9

Dauphas, N. (2007) Diffusion-driven kinetic isotope effect of Fe and Ni during formation of the Widmanstätten pattern. *Meteoritics & Planetary Science* 42, 1597–1613. https://doi.org/10.1111/j.1945-5100.2007.tb00593.x

Dauphas, N., Roskosz, M., Alp, E.E., Neuville, D.R., Hu, M.Y., Sio, C.K., Tissot, F.L.H., Zhao, J., Tissandier, L., Médard, E., Cordier, C. (2014) Magma redox and structural controls on iron isotope variations in Earth's mantle and crust. *Earth and Planetary Science Letters* 398, 127–140. http://doi.org/10.1016/j.epsl.2014.04.033

Davison, T.M., Ciesla, F.J., Collins, G.S. (2012) Post-impact thermal evolution of porous planetesimals. *Geochimica et Cosmochimica Acta* 95, 252–269. http://doi.org/10.1016/j.gca.2012.08.001

Greenwood, R.C., Barrat, J.A., Scott, E.R., Haack, H., Buchanan, P.C., Franchi, I.A., Yamaguchi, A., Johnson, D., Bevan, A.W.R., Burbine, T.H. (2015) Geochemistry and oxygen isotope composition of main-group pallasites and olivine-rich clasts in mesosiderites: Implication for the "Great Dunite Shortage" and HED-mesosiderite connection. *Geochimica et Cosmochimica Acta* 169, 115–136. https://doi.org/10.1016/j.gca.2015.07.023

Johnson, B.C., Sori, M.M., Evans, A.J. (2020) Ferrovolcanism on metal worlds and the origin of pallasites. *Nature Astronomy* 4, 41–44. https://doi.org/10.1038/s41550-019-0885-x

Jurewicz, A.J.G., Mittlefehldt, D.W., Jones, J.H. (1993) Experimental partial melting of the Allende (CV) and Murchison (CM) chondrites and the origin of asteroidal basalts. *Geochimica et Cosmochimica Acta* 57, 2123–2139. https://doi.org/10.1016/0016-7037(93)90098-H

Krawczynski, M.J., Van Orman, J.A., Dauphas, N., Alp, E.E., Hu, M. (2014) Iron isotope fractionation between metal and troilite: a new cooling speedometer for iron meteorites. In: *Lunar and Planetary Science Conference* 45, 2755.

Kruijer, T.S., Burkhardt, C., Borg, L.E., Kleine, T. (2022) Tungsten and molybdenum isotopic evidence for an impact origin of pallasites. *Earth and Planetary Science Letters* 584, 117440. https://doi.org/10.1016/j.epsl.2022.117440

McKibbin, S.J., Pittarello, L., Makarona, C., Hamann, C., Hecht, L., Chernonozhkin, S.M., Goderis, S., Claeys, P. (2019) Petrogenesis of main group pallasite meteorites based on relationships among texture, mineralogy, and geochemistry. *Meteoritics & Planetary Science* 54, 2814–2844. https://doi.org/10.1111/maps.13392

Mittlefehldt, D.W. (1980) The composition of mesosiderite olivine clasts and implications for the origin of pallasites. *Earth and Planetary Science Letters* 51, 29–40. https://doi.org/10.1016/0012-821X(80)90254-X

Ni, P., Chabot, N.L., Ryan, C.J., Shahar, A. (2020) Heavy iron isotope composition of iron meteorites explained by core crystallization. *Nature Geoscience* 13, 611–615. https://doi.org/10.1038/s41561-020-0617-y

Nichols, C.O., Bryson, J.F., Cottrell, R.D., Fu, R.R., Harrison, R.J., Herrero-Albillos, J., Kronast, F., Tarduno, J.A., Weiss, B.P. (2021) A time-resolved paleomagnetic record of main group pallasites: evidence for a large-cored, thin-mantled parent body. *Journal of Geophysical Research: Planets* 126, 7. https://doi.org/10.1029/2021JE006900

Polyakov, V.B., Mineev, S.D. (2000) The use of Mössbauer spectroscopy in stable isotope geochemistry. *Geochimica et Cosmochimica Acta* 64, 849–865. https://doi.org/10.1016/S0016-7037(99)00329-4

Poitrasson, F., Levasseur, S., Teutsch, N. (2005) Significance of iron isotope mineral fractionation in pallasites and iron meteorites for the core–mantle differentiation of terrestrial planets. *Earth and Planetary Science Letters* 234, 151–164. https://doi.org/10.1016/j.epsl.2005.02.010

Scott, E.R. (1977) Pallasites - metal composition, classification and relationships with iron meteorites. *Geochimica et Cosmochimica Acta* 41, 349–360. https://doi.org/10.1016/j.epsl.2005.02.010

Seifert, S., O'Neill, H.S.C., Brey, G. (1988) The partitioning of Fe, Ni and Co between olivine, metal, and basaltic liquid: An experimental and thermodynamic investigation, with application to the composition of the lunar core. *Geochimica et Cosmochimica Acta* 52, 603–616. https://doi.org/10.1016/0016-7037(88)90322-5

Tarduno, J.A., Cottrell, R.D., Nimmo, F., Hopkins, J., Voronov, J., Erickson, A., Blackman, E., Scott, E.R.D., McKinley, R. (2012) Evidence for a dynamo in the main group pallasite parent body. *Science* 338, 939–942. https://doi.org/10.1126/science.1223932

Walte, N.P., Solferino, G.F.D., Golabek, G.J., Silva Souza, D., Bouvier, A. (2020) Two-stage formation of pallasites and the evolution of their parent bodies revealed by deformation experiments. *Earth and Planetary Science Letters* 546, 116419. https://doi.org/10.1016/j.epsl.2020.116419

Wasson, J.T., Choi, B.G. (2003) Main-group pallasites: Chemical composition, relationship to IIIAB irons, and origin. *Geochimica et Cosmochimica Acta* 67, 3079–3096. https://doi.org/10.1016/S0016-7037(03)00306-5

Weyer, S., Anbar, A.D., Brey, G.P., Münker, C., Mezger, K., Woodland, A.B. (2005) Iron isotope fractionation during planetary differentiation. *Earth and Planetary Science Letters* 240, 251–264. https://doi.org/10.1016/j.epsl.2005.09.023

Windmill, R.J., Franchi, I.A., Hellmann, J.L., Schneider, J.M., Spitzer, F., Kleine, T., Anand, M. (2022) Isotopic evidence for pallasite formation by impact mixing of olivine and metal during the first 10 million years of the Solar System. *PNAS Nexus* 1, pgac015. https://doi.org/10.1093/pnasnexus/pgac015

Yang, J., Goldstein, J.I., Scott, E.R. (2010) Main-group pallasites: thermal history, relationship to IIIAB irons, and origin. *Geochimica et Cosmochimica Acta* 74, 4471–4492. https://doi.org/10.1016/j.gca.2010.04.016

Iron isotope evidence of an impact origin for main group pallasites

N.R. Bennett, C.K. Sio, E. Schauble, C.E. Lesher, J. Wimpenny, A. Shahar

Supplementary Information

The Supplementary Information includes:

1. MC-ICPMS Analyses of Pallasite Samples

Iron isotope compositions are known to be heterogeneous in iron and stony-iron meteorites where Widmanstätten patterns are present. Dauphas (2007) simulated the growth of kamacite and showed that the central regions of kamacite should have the same isotope composition as the bulk metal. Accordingly, X-ray maps were generated to target the central regions of kamacite for analyses (Fig. S-1). These X-ray maps were generated using a JEOL JSM-6500F SEM equipped with an Oxford X-Max 80 mm^2 Si drift detector at the Carnegie Institution for Science in Washington DC. X-ray maps for Esquel, Fukang, Seymchan, and Krasnojarsk were not produced but kamacite regions were identified in reflected light.

A NewWave micro-mill apparatus was used to drill into kamacite, olivine, and troilite phases, using a 300 μm diameter tungsten carbide drill bit purchased from Brasseler USA (catalogue# H52.11.003). Prior to drilling, drops of MQ water were placed on top of the target spot so that the drilled powders could be collected using a pipette. The slurry was then transferred to clean Savillex beakers. For the purpose of comparison, some samples were also hand-picked, by lightly crushing then selecting fragments with tweezers, for their olivine and metal fractions and analysed for their iron isotope compositions. This was done to determine the range of olivine-metal fractionations that can be obtained from untargeted sampling of the metal, and to confirm that micro-drilled olivine has the same iron isotope compositions as the bulk olivine hand-picked from the same meteorite. Digestion and column chemistry procedures follow those described in the literature (Craddock and Dauphas, 2011).

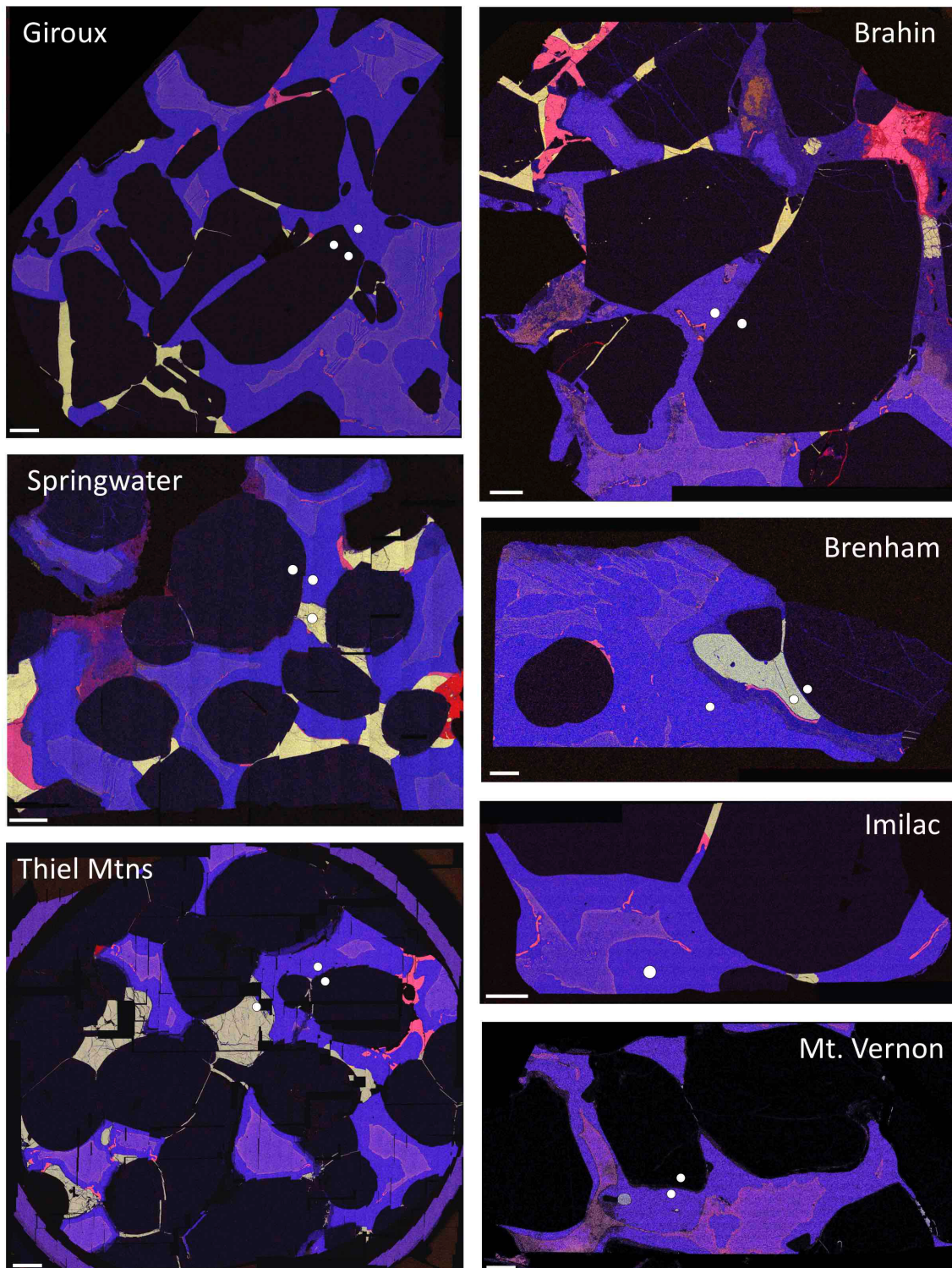**Figure S-1**   Positions of micro-drilled spots (white circles, 300 μm diameter), superposed on X-ray maps of pallasites investigated in this study. Scale bars are all 1 mm. Dark grains = olivine. Yellow = troilite. Bright pink = schreibersite. Bluish purple: kamacite. Pinkish purple = taenite. Note imperfect stitching for Springwater and Thiel Mtns. Location of drilled olivine spot for Imilac is outside the view of the X-ray map.

The Nu-Plasma II MC-ICPMS was used for iron isotope analyses at the Carnegie Institution for Science. Faraday cups H9, H6, Ax, and L3 were used to collect ion beams of ^{57}Fe, ^{56}Fe, ^{54}Fe + ^{54}Cr, and ^{53}Cr, respectively. Analyses were done in pseudo-high-resolution mode using a spray chamber and 10^{11} Ω amplifiers. Samples were bracketed by IRMM-524a, which has an identical isotopic composition to IRMM-014 (Craddock and Dauphas, 2011). Sample-standard concentration mismatch was always less than 5 %. The contribution of ^{54}Cr to the mass 54 signal was calculated assuming natural abundance of Cr isotopes (^{54}Cr = 0.249 $\times^{53}$Cr). The amount of Cr measured was insignificant, such that isotope compositions differ by less than 0.01 ‰ in δ^{56}Fe for data reduction done with or without the Cr correction (reported data have all been corrected for Cr). A single analysis represents the average of 5–9 replicates, each consisting of 20 cycles with a 4s integration time. Uncertainty is reported as the 2SE of the bracketing standard or the sample, whichever is the larger of the two. In cases where samples were analysed more than once, the weighted averages and weighted errors are given. Errors for Δ^{56}Fe$_{olivine-metal}$ are calculated as the quadratic sum of the 2SE errors for the olivine and metal analyses (Table S-4).

Comparison with previous measurements reveals, as expected, that variations in the measured olivine-metal fractionations arise from differences in the measurements of the bulk metal isotopic compositions (Fig. S-2; Table S-3). Some of the previous studies suffered from over-sampling of taenite, which can artificially shift Δ^{56}Fe$_{olivine-metal}$ to as low as -0.4 ‰ (Chernonozhkin *et al.*, 2016). One study reported positive Δ^{56}Fe$_{olivine-metal}$ and in this case, the metal contains troilite (Weyer *et al.*, 2005), which shifted the apparent Δ^{56}Fe$_{olivine-metal}$ to positive values. Targeted sampling thus eliminates the possibility of sampling highly fractionated taenite, as well as non-metal phases such as troilite.

2. Piston Cylinder Experiments

2.1 Experimental set-up

Starting materials were always metal plus Springwater olivine (Fa$_{18}$), prepared by crushing large olivine crystals handpicked under a binocular microscope. Olivine crystals were ground under isopropanol then sieved through a 37 µm mesh. Sieving was done to prevent the inclusion of large olivine grains in experimental starting materials that might prevent olivine-metal equilibrium from being achieved. The metal was prepared by first mixing 57.2 mg of high purity iron metal purchased from Alfa Aesar with 0.63 mg of ^{54}Fe-enriched metal purchased from Cambridge Isotopes. The mixture was heated in a graphite capsule at 1 GPa and 2000 °C for 15 mins, using a piston-cylinder press, to produce an isotopically spiked ingot. About 10 mg of this ingot was mixed with 990 mg of the Alfa Aesar iron powder and ground in an agate mortar to produce the final metal starting material. This spiked metal mixture was mixed with sieved Springwater olivine in a 15:85 olivine-metal ratio, then ground a final time under isopropanol using an agate mortar. The proportion of olivine was chosen to ensure extensive contact between olivine surfaces and the metal to promote olivine-metal equilibrium on reasonable timescales. Each experiment contained ~30 mg of the olivine-metal mixture. To test the effect of Ni on isotope fractionation, one experiment (72-hr) was doped with 12 wt. % Ni.

Experiments were performed using a Boyd-England type piston cylinder press with a 12.7 mm bore pressure vessel at UC Davis. Olivine-metal mixtures were encapsulated in graphite, then positioned in the hot spot of a graphite resistance heater using magnesia filler-pieces. The capsule was isolated from the graphite heater using a magnesia sleeve. The heater assembly is then surrounded by a BaCO$_3$ pressure medium and wrapped in Pb foil. Temperature in the experiments was monitored using a type-C thermocouple inserted axially so that the junction was located <0.5 mm above the sample capsule, which was separated from the thermocouple with a magnesia disk. Temperature was controlled manually by adjusting the power output to the heater. Automatic temperature control was not employed due to the long duration of some experiments and risk of thermocouple failure due to oxidation or contamination. All experiments were performed at 1 GPa and 1400 °C, with a 10 % friction correction applied to account for differences between oil pressure and sample pressure. Run durations were 3.5, 23, 48, 72, and 95 hours. Experiments were quenched by cutting power to the heater.

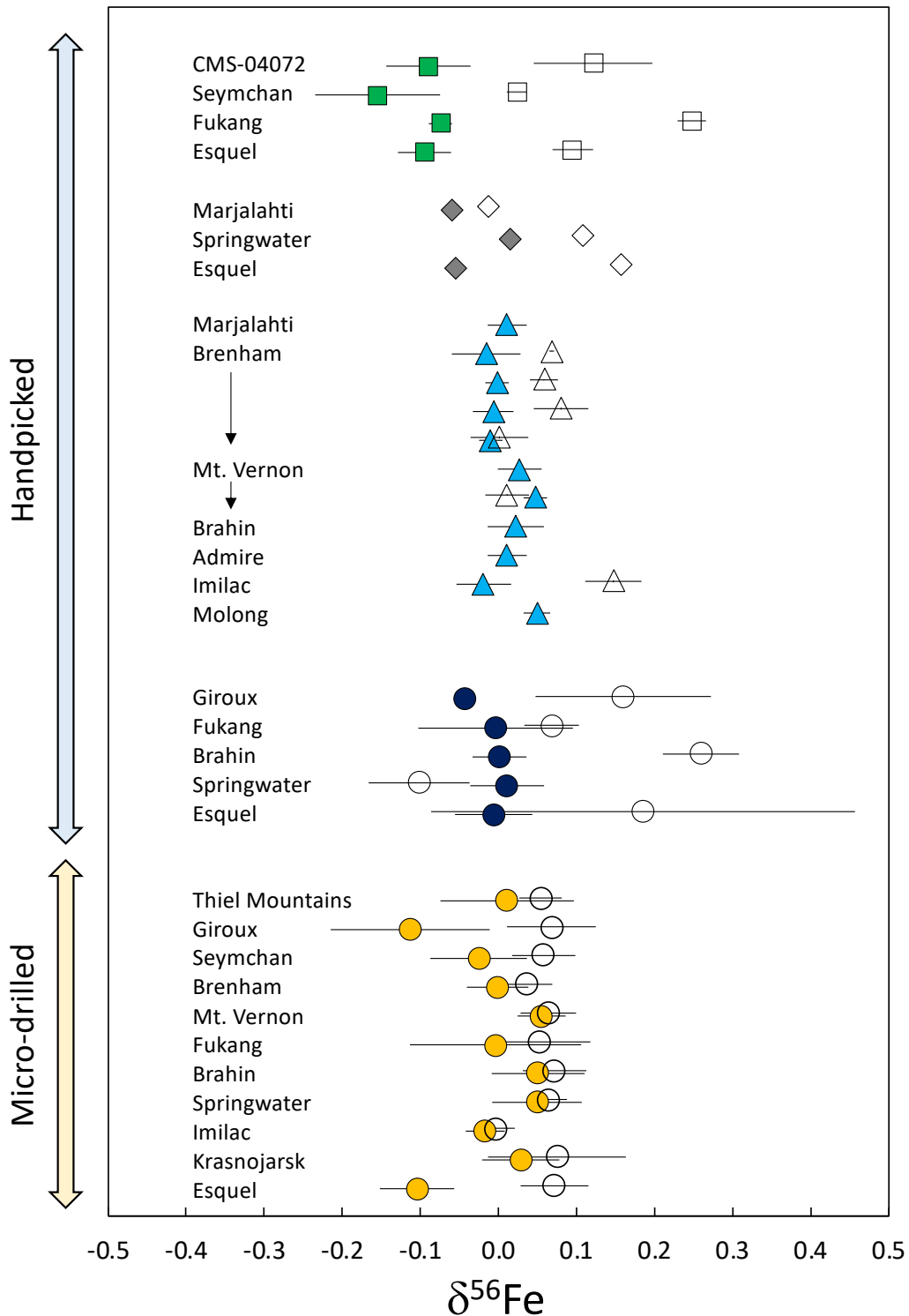**Figure S-2** "Bulk" metal (open symbols) and olivine (filled symbols) iron isotope compositions obtained by handpicking and micro-drilling sampling methods. Squares: Chernonozhkin *et al.* (2016). Diamonds: Poitrasson *et al.* (2005; error bars on δ^{56}Fe not reported). Triangles: Weyer *et al.* (2005); multiple fragments were analysed for Brenham and Mt. Vernon, some without pairing metal analyses. Circles: this study.

2.2 Chemical and textural characterisation of run-products

The 3.5, 23, 72, and 95 hr experiments were mounted in epoxy, cut longitudinally, then remounted and polished with SiC papers and 1 µm alumina powder prior to electron microprobe analysis at the Carnegie Institution for Science. Magnesiowüstite was formed in all experiments (Fig. S-3). The amount formed was calculated by noting the starting olivine composition of Fa_{18} and the equilibrated value of Fa_{23}. All Mg lost from olivine was assumed to have formed magnesiowüstite with a composition of $(Mg_{0.28}Fe_{0.72})O$. Using mass balance, we calculate that the mass ratio for magnesiowüstite:olivine is 0.12–0.18:1. Because $(Mg_{0.28}Fe_{0.72})O$ has 82 wt. % FeO and olivine has 22 wt. % FeO, ferrous iron is thus distributed between olivine and magnesiowüstite in an approximately 2:1 ratio. Thus, the experimentally determined fractionations correspond to that of olivine + magnesiowüstite mixture and metal. While this is not ideal, previous work has shown that ferrous oxides and olivine do not show resolvable iron isotope fractionation, especially when iron is 2+ and in octahedral coordination with oxygen. For example, the experimentally determined equilibrium $\Delta^{56}Fe_{ilmenite-olivine}$ is -0.01 ± 0.04 ‰ at 800 °C (Sossi and O'Neill, 2017), and the NRIXS-predicted $\Delta^{56}Fe_{magnesiowüstite-olivine}$ is -0.017 ± 0.020 ‰ at 1400 °C (Dauphas et $al.$, 2012). As a result, the presence of magnesiowüstite should not affect the magnitude or the direction of equilibrium olivine-metal fractionation.
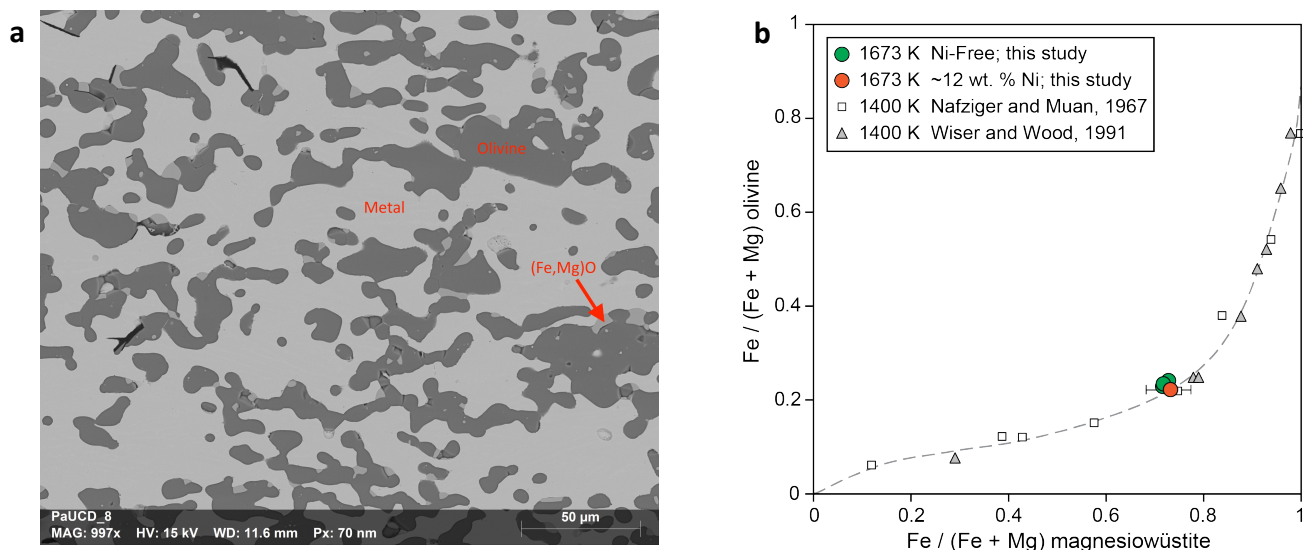
Figure S-3 **(a)** SEM image of the PaUCD8 run-product (23 hr), showing metal, olivine, and magnesiowüstite. **(b)** Equilibrium compositions of olivine and magnesiowüstite found in previous studies alongside data for our experiments. Excellent agreement is found between this study and previous work, indicating that chemical equilibrium is achieved rapidly in our experiments.

2.3 Phase separation and sample dissolution

For sample dissolution, each experiment was extracted from its epoxy mount and put in a clean 6 mL Savillex beaker filled with 0.5N HNO_3 for 4 days at room temperature. The supernatant was extracted and labelled "metal." The residue was rinsed 4 times in MQ water. Olivine and magnesiowüstite were obtained from leaching the solids using concentrated HNO_3 overnight at room temperature, and the supernatant labelled "olivine" for simplicity. All the "olivine" fractions were analysed for their Mg/Fe ratios using the Element XR at the Lawrence Livermore National Laboratory. For each sample, the expected Mg/Fe ratio was calculated knowing the relative amounts of olivine and magnesiowüstite present. Lower than expected Mg/Fe ratios are attributed to metal contamination, which are 6, 0, 19, 44, and 65 % for the 3.5, 23, 48, 72, and 95 hr experiments. The amount of contamination tends to increase with longer experimental duration. We attribute this to progressive recrystallisation of the graphite capsule with time. In all experiments, graphite forms inwardly oriented crystals at the metal-capsule interface, most likely fluxed by molten iron that has low viscosity and contains 4.7 wt. % carbon at our experimental conditions. In long duration experiments, these graphite crystals form an interlocking network that encloses a small fraction of the metal, potentially preventing its complete digestion during the

0.5N HNO$_3$ leach step (Fig. S-4). Corrections to $\Delta^{56}Fe_{olivine-metal}$ to account for the presence of metal in the olivine fraction are <0.038 ‰. The data reported in the main text include all uncertainties arising from these corrections.
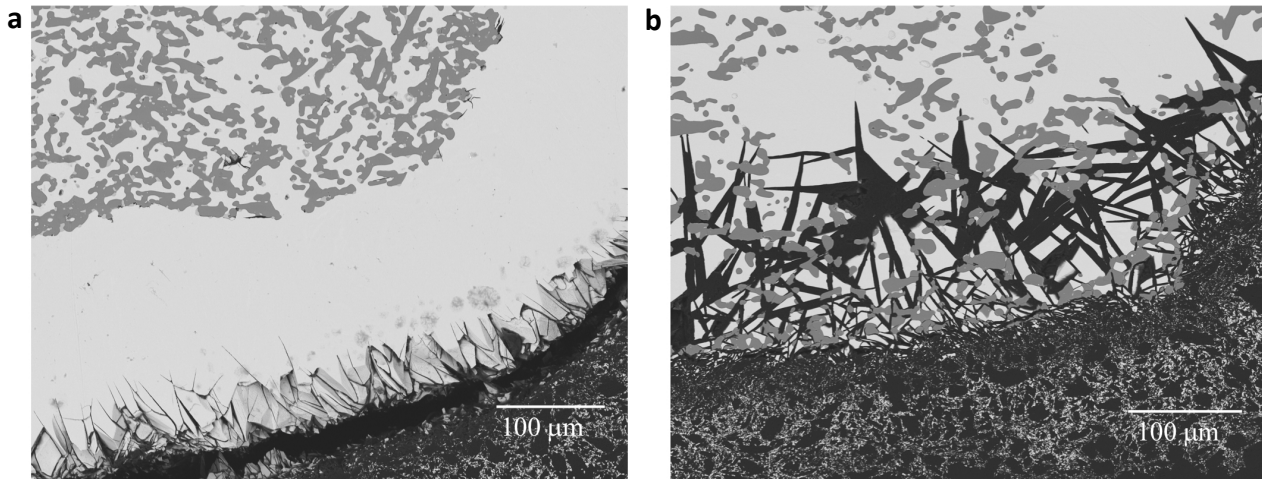
Figure S-4   SEM images showing the edges of experimental run-products. **(a)** PaUCD7 (3.5hr) showing limited recrystallisation of graphite near the metal-capsule interface. **(b)** PaUCD11 (72hr) showing more extensive recrystallisation of graphite into the metal phase.

2.4. Effect of leaching on iron isotope compositions

Acid leaching of olivine may fractionate isotopes such that the supernatant may not have the same isotope composition as the residue. To confirm that leaching did not affect our results, time series tests were performed on 3 separate sets of powdered San Carlos olivine, each weighing ~7 mg. These test samples were leached in 0.5N HNO$_3$ for 1, 2, and 3 days at room temperature. After the requisite number of days was reached, each supernatant was pipetted into clean Savillex beakers and labelled "0.5N HNO$_3$." Then, the residues were rinsed 4 times with MQ-water, as done for the piston cylinder experimental charges. Concentrated HNO$_3$ was then added to each residue and left for 1 day at room temperature. These supernatants were transferred to clean Savillex beakers and labelled "conc HNO$_3$." The residues were again rinsed 4 times with MQ-water, then digested in HF-HNO$_3$ at 120 °C overnight. These were labelled "residue." About 7 mg of the fresh San Carlos olivine powder was digested directly in HF-HNO$_3$. All of these samples were processed through column chemistry in the same way as the piston cylinder experimental charges. For these leaching tests, fresh San Carlos olivine was used as the bracketing standard. Shown in Figure S-5 is evidence that except for the 1-day "0.5N HNO$_3$" sample, all samples show no isotopic fractionation from the fresh sample. This shows that while the light isotopes are preferentially leached in 0.5N HNO$_3$, the longer durations (>2 days) are not affected. As the piston cylinder samples were leached for 4 days in 0.5N HNO$_3$, the test confirms that our leaching procedure does not fractionate iron isotopes. A similar result was obtained by Poitrasson *et al.* (2009).

2.5 MC-ICPMS Analyses of Experimental Samples

Isotopic measurements for the leaching tests and for the experimental run-products were made using the Neptune Plus MC-ICPMS at the Lawrence Livermore National Laboratory using set-up and routine described in Craddock and Dauphas (2011). Cr-correction procedure were performed as described in Section 1; the corrections were also negligible. For geostandards and metal samples, IRMM-524a was used as the bracketing standard. For the experimental "olivine" samples, the corresponding metal fractions were used as the bracketing standard to minimise uncertainty (*i.e.* to avoid having to calculate a quadratic sum for error). Geostandards were processes along with samples and our data are in excellent agreement with literature values (Table S-5).
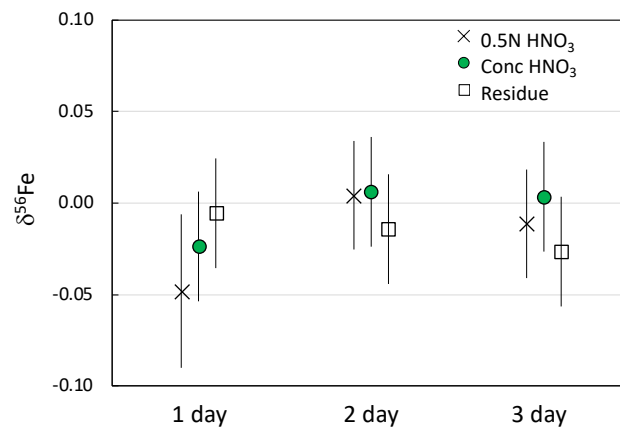
Figure S-5   Effect of leaching on the iron isotope compositions of olivine. The number of days refers to the duration of leaching in 0.5N HNO$_3$. After this first step of leaching, all remaining residue was leached again in concentrated HNO$_3$ for a day. After this second step of leaching, the residue was digested in HF+HNO$_3$.

2.6 Piston Cylinder Experimental Results

In all experiments, the metals in the post-run products have an identical isotopic composition, which is different to the aliquot of digested starting material. Iron loss to the capsule is ruled out because iron isotope compositions of the run-product metal are identical regardless of run duration. Instead, the difference between starting material and post-run products can be reconciled by isotopic inhomogeneity in the starting material at the mg-scale. Less than a few mg of metal starting materials were digested for isotopic analyses, whereas each experiment contained >30 mg of metal.

Electron probe analyses show that chemical equilibrium was achieved in 3.5 hr, but isotopic equilibrium is attained only after >23 hr. The longest three durations show that the "olivine" fractions lie on the secondary fractionation line (Fig. S-6) and they display a constant $\Delta^{56}Fe_{olivine-metal}$ (Fig. S-7). Even with metal contamination, that would drive $\Delta^{56}Fe_{olivine-metal}$ toward zero, the "olivine" fractions are consistently heavy. This shows that even with the difficulty of obtaining pure phases for analysis, we were able to constrain the direction of olivine-metal fractionation. As the three experiments with the longest durations show identical fractionations, the weighted average $\Delta^{56}Fe_{olivine-metal}$ values are calculated to be 0.030 ± 0.022 ‰, and 0.054 ± 0.030 ‰ uncorrected and corrected for metal contamination, respectively. We observe that Ni has no measurable effect on the Fe isotope fractionation and that, at equilibrium, olivine is isotopically heavy compared to metal.

The direction of Fe isotope fractionation found in our experiments may be compared to those reported by Elardo and Shahar (2017), in which they measured Fe isotope fractionation between silicate melt and metal equilibrated at 1850 ºC. It is noteworthy that in Elardo and Shahar's experiments, the silicate is a molten peridotite-like melt and the temperature was 450 ºC higher than in our study. Similar to our study, they conducted experiments at 1 GPa and used graphite capsules so that their metal is also saturated in carbon. Four of their experiments are Ni-free and yield a weighted average $\Delta^{56}Fe_{silicate-metal}$ of 0.038 ± 0.024 ‰.
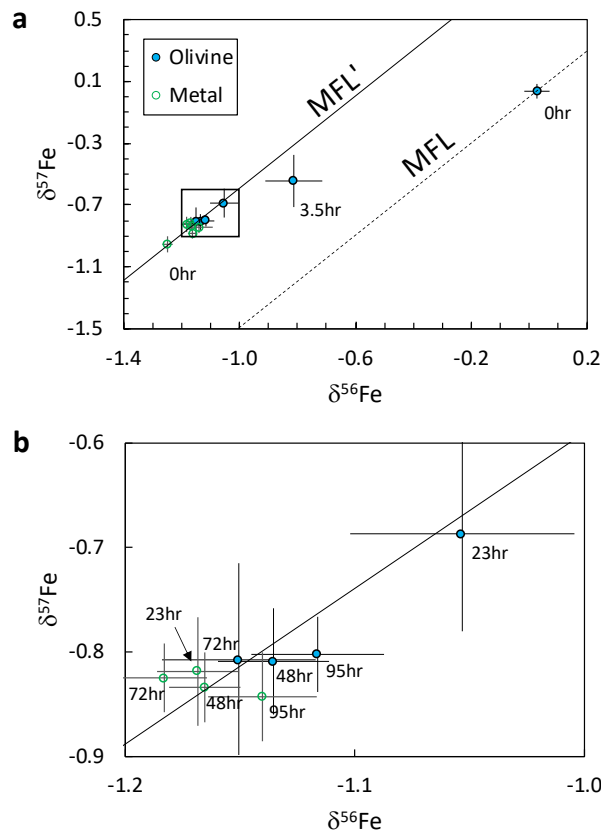
Figure S-6   Three-isotope plots showing the approach to equilibrium. MFL denotes the terrestrial mass fractionation line. MFL' denotes the secondary mass fractionation, defined by the addition of ^{54}Fe-enriched spike, which was added to the metal. Values plotted are raw data, uncorrected for metal contamination. **(b)** Depicts the area within the black outlined box in **(a)**.

The results of Ni-free experiments performed by Elardo and Shahar (2017) are therefore in good agreement with our study; recording that, at equilibrium, silicate is isotopically heavier than metal. However, this agreement does not persist to higher Ni contents, where Elardo and Shahar (2017) found a negative relationship between Ni/(Ni + Fe) in the metal and Δ^{56}Fe$_{silicate-metal}$. In other words, the addition of Ni to the metal caused the silicate-metal fractionation to change sign, but this is not observed in our experiments.

Regressing through the data of Elardo and Shahar (2017), we calculated an iron sublattice force constant difference (ΔF) of 267 N/m between Ni$_{12}$Fe$_{88}$ (pallasitic metals) and silicate (Δ^{56}Fe = 2853x $\Delta F/T^2$, where T is in Kelvin; Dauphas *et al*., 2014). All measured materials in the Solar System, synthetic or otherwise, have force constants between 97 and 351 N/m at pressures of less than 1 GPa (see compilations in Dauphas *et al*., 2012, 2014; Roskosz *et al*., 2015; Shahar *et al*., 2016; Liu *et al*., 2017, Smith *et al*., 2021; Nie *et al*., 2021). Therefore, the largest possible ΔF between any two materials is 254 N/m. The ΔF between Ni$_{12}$Fe$_{88}$ and olivine we found in this study is 42 N/m, which is well within the expected range. The ΔF of 267 N/m implied by the results of Elardo and Shahar (2017), however, is unexpectedly large and thus challenging to explain.

Lastly, Bourdon *et al*. (2018) used a simplified approach to estimate olivine-metal fractionation factors based on charge, coordination number, and Debye temperature. They also found that, at equilibrium, olivine is isotopically heavier than metal. However, they do not give details of their model parameters, and do not specify whether the metal they consider has a bcc or fcc structure. As a result, although in qualitative agreement, a rigorous comparison of our results with those of Bourdon *et al*. (2018) is not possible.

a

b
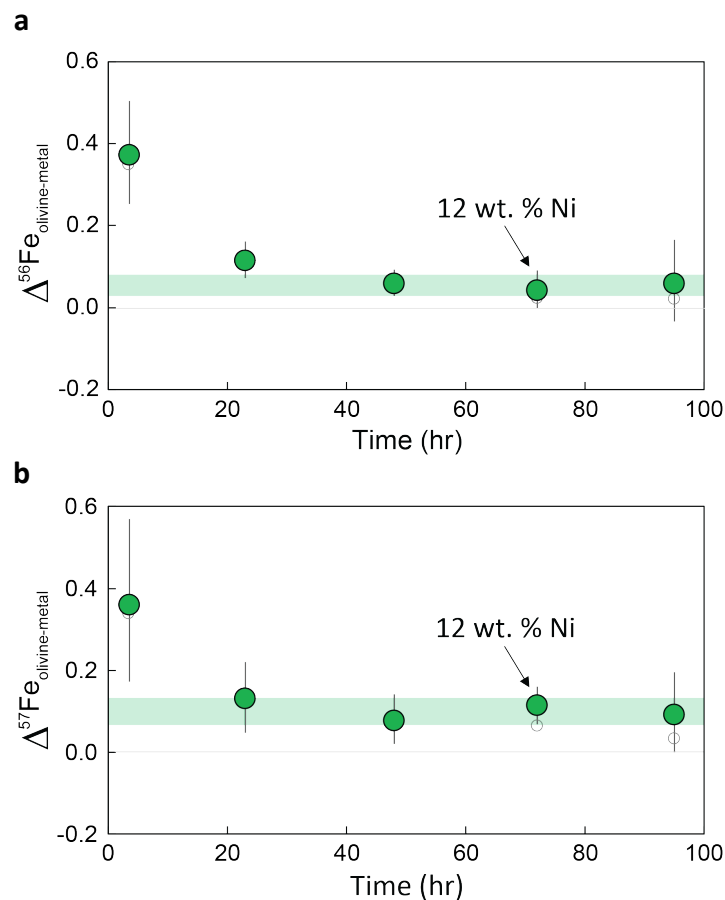
Figure S-7   Time series experiments showing data corrected (filled green circles) and uncorrected (empty grey circles) for metal contamination. Individual error bars display the upper and lower limits allowed given uncertainties in the metal contamination corrections. Green bands show the weighted averages calculated using the corrected data for the longest 3 experiments: $\Delta^{56}Fe_{olivine-metal}$ = 0.054 (+0.027, -0.024) ‰ and $\Delta^{57}Fe_{olivine-metal}$ = 0.099 (+0.036, -0.033) ‰. The addition of 12 wt. % nickel in the metal has no resolvable effect on the isotope fractionation.

2.7 Bonding Environment of Iron in Molten Metal in Piston Cylinder Experiments

As the olivine-metal assemblages were enclosed in graphite capsules, the metal was saturated in carbon and is thus molten with 4.7 wt. % C. Studies have shown that the presence of carbon has no bearing on the structure of the molten metal up to 5 wt. % C (Belashchenko *et al.*, 2011). This is corroborated by the fact that the nearest Fe-Fe interatomic distances are 2.58 Å in molten Fe (ambient pressure; 1560–1650 °C; Waseda and Ohtani, 1974) and 2.56 Å in molten Fe-C (2.2 GPa; 1327 °C; 3.5 wt. % C; Shibazaki *et al.*, 2015). These distances are close to that of the fcc-metal (2.55 Å) but distinguishable from that of the bcc-metal (2.05 Å). In addition, the coordination number (CN) of the molten iron at ambient pressure is ~11 (Waseda and Ohtani, 1974), close to that of fcc-metal (CN = 12), but far from that of bcc-metal (CN = 8). The similarity in interatomic distances and CN suggests a similar bond strength between fcc-Fe and molten Fe at low pressure.

2.8 Mechanism for Experimental Olivine-Metal Equilibrium and Olivine Rounding

Isotopic equilibration presumably is achieved in our experiments via solid-state diffusion in olivine and recrystallisation of olivine in molten metal. Recrystallisation was responsible for isotopic exchange in the studies of Matsuhisa *et al.* (1978), Shahar *et al.* (2008), and Trail *et al.* (2019). In those experiments, isotopic exchange occurs at a temperature low enough to inhibit volume diffusion. In this case, evolution toward equilibrium is observed as a mixing line. However, in the case of volume diffusion, the evolution follows a trajectory that is different from the mixing line. To

model this type of isotopic exchange, we modelled the evolution of δ^{56}Fe in olivine as a function of time, for a 10 μm spherical radius olivine with an initial composition of 0‰ subject to an infinite reservoir of -1.15 ‰ in δ^{56}Fe and -0.80 ‰ in δ^{57}Fe. The isotope effect for diffusion $\beta = 0.16$ was used (Sio *et al.*, 2018), where $D_1/D_2 = (m_2/m_1)^\beta$ (D = diffusivity; m = mass). When diffusion has affected the core of the olivine, we predict that the bulk olivine composition will be isotopically light compared to the metal, and thus δ^{56}Fe overshoots the secondary mass fractionation line (MFL'; Fig. S-8). This was not observed for our experiments, suggesting that recrystallisation, *i.e.*, migrating olivine-metal boundaries, has played a dominant role for reaching isotopic equilibration. Moreover, our modelling shows that diffusive effects would produce isotopically light olivine - the opposite of what is observed. Note that the equilibrium iron isotope fractionation reported does not rely on extrapolation on the 3-isotope diagram, because our time-series demonstrates that isotopic equilibrium was achieved in the three longest experiments.
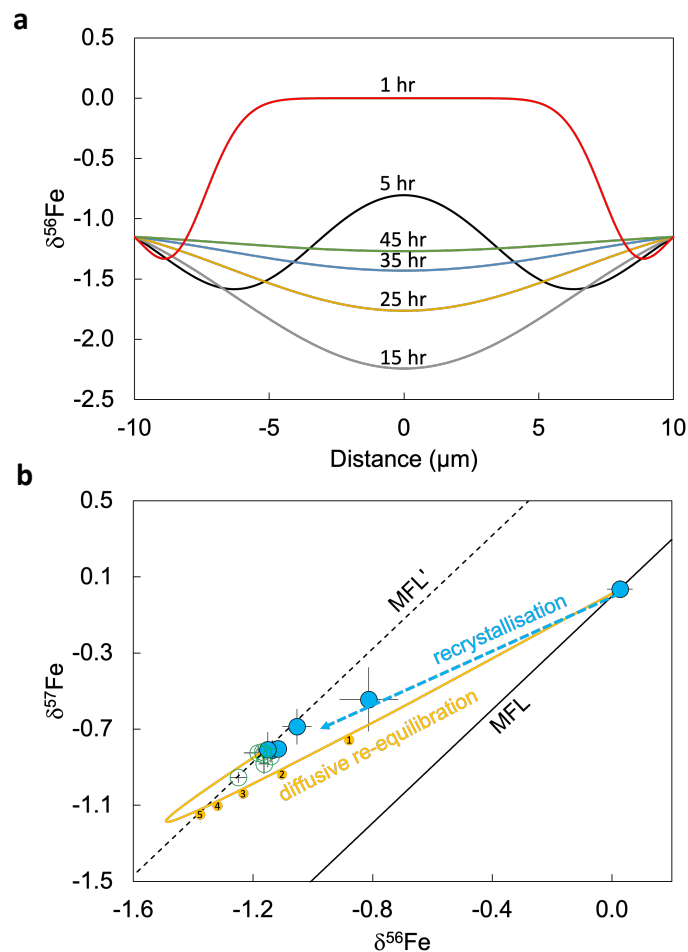
Figure S-8   **(a)** Modelled time evolution for the iron isotopic profile in olivine if re-equilibration is achieved via diffusion only (*i.e.*, no moving boundary). **(b)** Yellow curve shows evolution of bulk olivine δ^{56}Fe and δ^{57}Fe, calculated by integrating modelled intra-crystalline profiles in 0.05 micron increments; snapshots for the first 5 hr are marked at the 1-hr increment. If equilibration is achieved via volume diffusion only, then bulk olivine compositions are expected to overshoot the MFL' before arriving at the equilibrium compositions. As this is not observed, our experimental data suggests that equilibration predominately occurred via olivine recrystallisation.

Recrystallisation of olivine in a metallic matrix has been studied experimentally (Saiki *et al.*, 2003; Guignard *et al.*, 2012; Solferino *et al.*, 2015). Direct comparison with the experiments of Saiki *et al.* (2003) and Guignard *et al.* (2012) is difficult because their experiments were conducted below the metal solidus temperature. For our experiments

involving solid olivine and molten metal, recrystallisation can occur by grain boundary migration and coalescence, the latter of which may be described by the sintering of two grains "dragged" by movement of the matrix phase (Guignard *et al*., 2012). Solferino *et al*. (2015) found that rounding occurs quickly when olivine grains are submerged in a molten Fe-S matrix. Our study agrees with the results of Solferino *et al*. (2015), who showed that olivine fully recrystallised and chemically equilibrated with molten metal in ~3 hours. However, here we show that under our experimental conditions, isotopic equilibration takes >23 hours to achieve. It is therefore possible, that volume diffusion still plays a role in the approach to isotopic equilibrium.

Pallasites contain both rounded and angular olivine grains. Both our experiments, and those of Solferino *et al*. (2015) show that rounding is quickly achieved at the micron-scale and the olivine texture remains essentially unchanged in the longer duration experiments. It is therefore difficult to speculate on the timescales required to round a mm- or cm-sized olivine when submerged in molten metal. Saiki *et al*. (2003) calculated that it would take 7–241 Myr to round a 5 mm radius olivine in a solid Fe-Ni alloy at 1400–1200 °C. However, this timescale is expected to decrease significantly with the addition of S (Saiki *et al*., 2003; Solferino *et al*., 2015). To constrain the timescale required to produce large, rounded, olivine grains, the kinetics will have to be studied using larger olivine grains in Fe-Ni-S metal at temperatures both above and below the solidus of the metal. This approach may, in the future, yield valuable constraints on the thermal history of pallasite formation.

3. Olivine, Awaruite, and Tetrataenite Force Constant Calculations

The density functional theory (DFT) models generated for the present study are similar to the ones constructed by Blanchard *et al*. (2009), using the PBE functional (Perdew *et al*., 1996), projector augmented wave datasets from the PSLibrary (Dal Corso, 2014 ; v. 0.3.1 for O and Fe; https://dalcorso.github.io/pslibrary/), ultrasoft pseudopotentials from the GBRV library (Garrity *et al*., 2014; v1.5 for Mg, Si, and Ni; https://www.physics.rutgers.edu/gbrv/), and plane wave basis sets. We did not use a Hubbard U correction. The kinetic energy cut-offs for the plane wave basis sets are fixed at 90 Rydberg (1225 eV) for wavefunctions and 1080 Rydberg (14694 eV) for the charge density and potential (Garrity *et al*., 2014). Electronic wave vectors of single olivine unit cells are sampled on a 4×2×4 offset Monkhorst-Pack grid, wave vectors for 2×1×1 olivine supercells are sampled on an offset 2×2×4 grid. Awaruite and tetrataenite unit cells are sampled on offset 18×18×18 and 26×26×18 electronic wave vector grids, respectively, with 0.01 Ryd (0.14 eV) Gaussian smearing. Version 6.5 of the Quantum Espresso software package (Giannozzi *et al*., 2009) is used for all model calculations.

For iron carbonate and oxide crystals, Blanchard *et al*. (2009) estimate vibrational frequency scale factors of 1.061-1.083, consistent with scale factors of ~1.06 found for Sr- and Ca-bearing crystals (Widanagamage *et al*., 2014), and slightly larger than found for pure forsterite (Schauble, 2011) (~1.03-1.04). A test calculation of Raman-active vibrational frequencies in siderite ($FeCO_3$) indicates that the DFT models in our study are in reasonable agreement with the Blanchard *et al*. (2009) calculations (a linear regression gives $R^2 > 0.998$ and a slope of 0.995), and scale factors should be similar. We therefore adopt a frequency scale factor of 1.06 ± 0.03 for the present calculation of Fe-isotope fractionation in olivine. This corresponds to a force constant scale factor of $(1.06 \pm 0.03)^2 = 1.124 \pm 0.06$ for olivine. A frequency scale factor of 0.950 ± 0.02 is used for awaruite and tetrataenite, based on a best-fit proportional regression to phonon frequencies in bcc-Fe measured at several high-symmetry wave vectors by inelastic neutron scattering method (Brockhouse *et al*., 1967). This corresponds to a force constant scale factor of 0.903 ± 0.04 for awaruite and tetrataenite, which may represent an underestimation of error because the scale factor was determined for bcc-Fe, instead of the specific metal phases.

Modelled olivine structures contain one Fe(II) atom in either an M1 site or an M2 site in each unit cell. All Fe-substituted structures are allowed to relax to find the nearest (local) minimum-energy configuration, using a pure forsterite model as the initial guess structure. These models correspond to an $Fa_{12.5}$ stoichiometry, with a 1:7 Fe:Mg atomic ratio. The effect of varying Fe:Mg ratios on isotopic partitioning is not addressed by these models. Ferromagnetic structures are

assumed in all olivine models – magnetic coupling between iron sites will likely be weak in such Fe-poor structures, and the effect of magnetic structure is expected to be small relative to other sources of uncertainty. Force constants are estimated by numerical displacement for single unit cell domains (28 atoms) and 2×1×1 supercells (56 atoms) that are doubled along the shortest unit cell dimension, which corresponds to the a-axis in the standard Pbnm setting of space group #62 used for olivine. Force constants for awaruite and tetrataenite are estimated from the effects of $^{56}Fe/^{54}Fe$ substitution on the phonon density of states for each structure (Elcombe and Hulston, 1975), calculated with linear response theory on offset 3×3×3 (awaruite) and 3×3×2 (tetrataenite) phonon wave vector grids.

Estimated average force constants in 2×1×1 supercells are 151 N/m and 131 N/m for M1 and M2 substituted olivines, before scaling, and 170 ± 10 N/m and 148 ± 9 N/m, respectively, after scaling. The uncertainties given here only consider variations in the force constant scale factor. Cruder estimates based on simple unit cells are 149 N/m and 130 N/m for M1 and M2, respectively, before scaling, averaging 1 % lower than the supercell models. This similarity suggests that the 2×1×1 supercell domain is large enough to estimate the force constant for displacement of a single isolated atom with reasonable accuracy.

The site partitioning behaviour of Fe(II) in olivine has been extensively investigated in previous studies. For the present study, we are assuming the partitioning behaviour is similar to that measured in the closest compositional analogue to our model structures, the Fa_{12} olivine sample measured by Heinemann *et al.* (2007). In this sample the K_D varies only slightly (1.13 ± 0.04) over the 500–750 ºC temperature range. This corresponds to 52–54 % of Fe occupying the M1 site, and 46–48 % occupying the M2 site, and a site-weighted, average force constant of 159 ± 10 N/m.

4. Closure Temperature for Iron in Olivine

Closure temperature can be defined as the temperature when diffusion of an element effectively ceases and the bulk isotopic composition of a mineral no longer changes with further cooling (Dodson, 1973). Closure temperature, T_C, can be calculated using Eq. 23 in Dodson (1973):

$$\frac{E}{RT_C} = ln\left(-\frac{ART_c^2 D_0/a^2}{EdT/dt}\right)$$　　　　　　　　　　Eq. S-1

with the parameters defined as in Table S-1 for pallasitic olivine.

Table S-1 Parameters for calculating pallasite olivine closure temperature.

Parameter	Description	Value(s)
E	Activation energy for diffusion	220,000 J
R	Gas constant	8.3145 J K^{-1} mol^{-1}
A	Geometry factor	55 for a sphere
D_0	Pre-exponential factor in Arrhenius equation	$10^{-8.85}$ m^2/s
a	Radius	2 mm
dT/dt	Cooling rate	7 K/Myr

Mg-Fe interdiffusion in olivine has a fast diffusion direction, along [001], that is six times larger than the slow diffusion directions, along [100] and [010] (Dohmen and Chakraborty, 2007). To obtain the lowest closure temperature, the fast diffusivity (*i.e.*, D_0 along [001]) is used. D_0 also depends on Fa# (= 100 × atomic Fe/(Fe+Mg) in olivine); the typical MGP composition of Fa_{12} is used in this calculation (Buseck, 1977). For an average MGP cooling rate of 7 °C/Myr (determined for cooling below 650 °C; Yang *et al.*, 2010), the closure temperature is 656 °C. This closure temperature is shown as the red dashed line on the Fe-Ni phase diagram in Figure S-9. For the Ni contents of MGP metals (8.2 – 13.6 wt. % Ni; Wasson and Choi, 2003), olivine reaches its closure temperature before significant kamacite formation occurs. Olivine-metal equilibrium, if it occurred, would therefore be between olivine and either fcc- or liquid-metal.

Note that the presence of phosphorus in pallasites depresses the kamacite-taenite solvus to lower temperatures than shown in Figure S-9, further separating the olivine closure temperature from kamacite nucleation temperatures (Yang *et al.*, 2010).
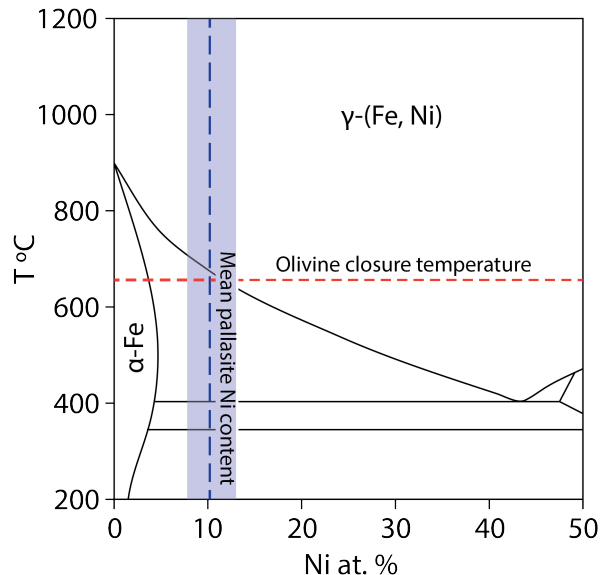
Figure S-9 Simplified Fe-rich portion of the Fe-Ni phase diagram showing the calculated olivine closure temperature (red line; see text for details). Olivine-metal equilibrium would occur above this temperature, which for the range of Ni contents recorded in pallasite meteorites (shaded blue region), is largely above the temperatures where kamacite (α-Fe) forms from taenite (γ-FeNi).

5. The Effect of Mass Exchange at Low Temperature on Iron Isotope Fractionations

Olivine-metal isotopic fractionations could be overprinted after equilibration, by mass transfer between phases. At ~650 ºC, iron diffuses 5 and 8 orders of magnitude faster in troilite than kamacite and olivine, respectively (Condit *et al.*, 1974; Dauphas *et al.*, 2007; Dohmen and Chakraborty, 2007). As iron diffusion in troilite and kamacite are much more rapid than in olivine, iron isotopic exchange between the former phases may continue well after exchange with olivine effectively ceases. To constrain the extent of this effect on the approximation that $\delta^{56}Fe_{kamacite} \approx \delta^{56}Fe_{bulk\ metal}$, we measured troilite micro-drilled from Brenham, Thiel Mountains, and Springwater pallasites. The resulting $\delta^{56}Fe_{troilite}$ values are -0.223 ± 0.034 ‰, -0.456 ± 0.027 ‰, and -0.445 ± 0.050 ‰, respectively. Because the average metal-to-troilite modal proportion is 17:1 (Buseck, 1977; suggesting kamacite-to-trolite modal ratio of ~15:1) and kamacite is more Fe-rich than troilite, the net effect on the isotopic composition of kamacite is <0.02 ‰. Such a correction cannot account for the disequilibrium $\Delta^{56}Fe_{olivine-metal}$ signature measured in MGP.

Second, small chemical variations have been reported at the rim of pallasitic olivine. Chernonozhkin *et al.* (2017) examined these variations in Brahin, Brenham, Esquel, Fukang, Imilac, and Seymchan pallasites in contact with metal, but could not resolve any Fa# profile except for Esquel. They measured olivine rim and core compositions of $Fa_{11.05}$ and $Fa_{11.23}$, respectively. This may represent net diffusion of iron from olivine to the surrounding metal. Chemical diffusion will generally fractionate isotopes but the extent of fractionation depends on the magnitude of the compositional contrast. A small compositional contrast will result in a correspondingly small isotope fractionation, because diffusive flux is small and isotopic signals are therefore diluted by a large background of unfractionated material. At such a small compositional contrast, the iron isotope fractionation driven by chemical diffusion is calculated to be less than 0.03 ‰ (Fig. S-10; calculated using Eq. A12 from Sio *et al.* (2018) with $\beta = 0.16$). Note that this is the maximum fractionation at a single point in the diffusion profile and, accounting for mass balance, would have a negligible effect on the bulk composition of the olivine crystal.
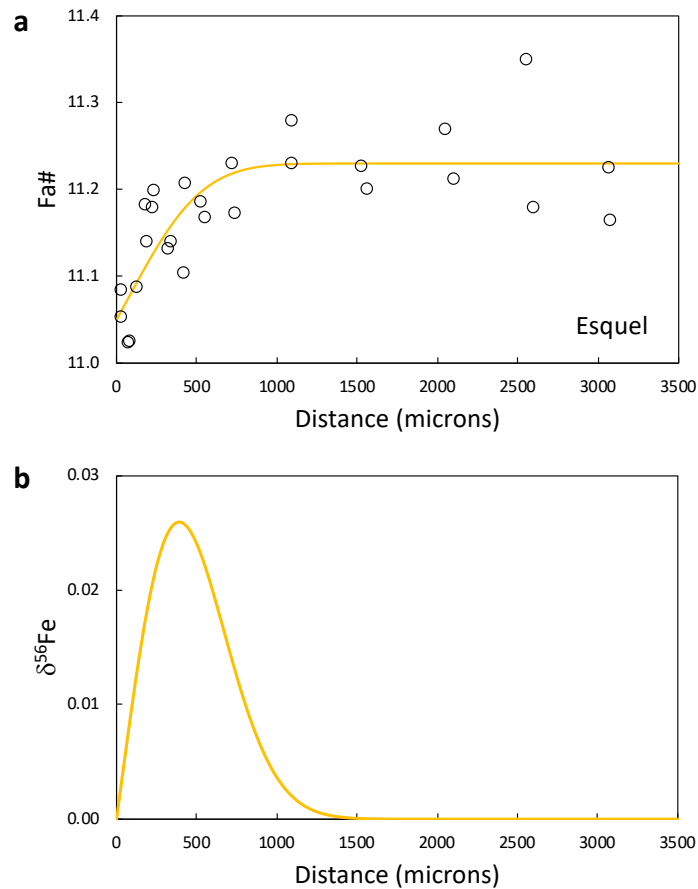
Figure S-10 **(a)** Our fit to the chemical profile in Esquel olivine reported by Chernonozhkin *et al.* (2017). x = 0 marks the kamacite-olivine interface. **(b)** Curve shows the associated isotope profile.

6. Models of Planetesimal Cooling and Olivine-Metal Equilibration

We coupled models of planetesimal cooling with calculations of Fe-isotope diffusion in olivine, to establish the range of conditions under which olivine and metal can remain unequilibrated. We employed a 1-D cooling model following the approach used in Bryson *et al.* (2015). For a spherically symmetric body (the planetesimal), losing heat by conduction, the temperature change with time (*t*) at radius (*r*) is given by:

$$T_r^t = \kappa \delta t \left(\frac{1}{r\delta r} \left(T_{r+\delta r}^{t-\delta t} - T_{r-\delta r}^{t-\delta t} \right) + \frac{1}{\delta r^2} \left(T_{r+\delta r}^{t-\delta t} - 2T_r^{t-\delta t} + T_{r-\delta r}^{t-\delta t} \right) \right) + T_r^{t-\delta t} \qquad \text{Eq. S-2}$$

where T is temperature (K), and κ is the thermal diffusivity. The planetesimal body was modelled as comprising three layers: a metallic core, silicate mantle, and megaregolith. Parameter units and the physical properties used for each layer in the model are given in Table S-2.

The core was modelled as an isothermal liquid, that decreased with temperature in each time step according to the amount of heat lost across the core-mantle boundary (CMB):

$$\Delta T = \frac{3k_m \frac{\delta T}{\delta r}\big|_{r_C} \delta t}{\rho_C C_{p_C} r_C} \qquad \text{Eq. S-3}$$

where ΔT is the temperature change of the core in each time step, k_m is the thermal conductivity of the mantle, ρ_c is the density of the core, and C_{p_c} is the specific heat capacity of the core. After the onset of core crystallisation (1200 K), the core temperature is fixed until the heat extracted across the core mantle boundary exceeds the total latent heat of core crystallisation $\left(Q_{L_C}\right)$. The heat extracted across the core-mantle boundary in each time step (ΔQ_{CMB}) is calculated from:

$$\Delta Q_{\text{CMB}} = 4\pi r_C^2 k_m \frac{\delta T}{\delta r}\bigg|_{r_C} \delta t \qquad \text{Eq. S-4}$$

and the total latent heat of core crystallisation $\left(Q_{L_C}\right)$ is given by:

$$Q_{L_C} = \frac{4}{3}\pi r_C^3 \rho_C L_C \qquad \text{Eq. S-5}$$

where L_C is the specific latent heat of core crystallisation (see Table S-2). Once core crystallisation is complete, the simulation is terminated. This was due to the palaeomagnetic constraint that olivine-hosted magnetic inclusions and cloudy zones in the pallasite metal formed in the presence of a geodynamo (Tarduno *et al*., 2012; Bryson *et al*., 2015). Because the cloudy zones formed at < 600 K (Yang *et al*.,1996), which is below the closure temperature for olivine, the period following core crystallisation was not considered as relevant for isotopic equilibration.

Temperature-time histories for different mantle depths were extracted from this model and used as conditions for Fe exchange between olivine and metal. Our diffusive equilibrium models assume a spherical olivine grain surround by an infinite, well-mixed, reservoir of iron metal. The olivine was given a diameter of 4 mm, the mean olivine grain size observed in pallasite meteorites (Wasson and Choi, 2003). Based on our analyses of natural samples (Fig. S-2), the initial δ56Fe of the olivine was assumed to -0.05 ‰, subject to a fixed boundary condition of δ56Fe = +0.05 ‰ (*i.e*., the equilibrium value). Because the typical uncertainty for δ56Fe analyses is ±0.05 ‰, we stop the chemical diffusion model when the core of the olivine displays a composition of 0 ‰, at which point the olivine is considered equilibrated. This approach extends the calculated equilibrium curve to the maximum plausible depths and reflects a conservative approach to ruling-out a core-mantle boundary origin for MGP.

The diffusivity of Fe in olivine is taken from Dohmen and Chakraborty (2007) and is temperature dependent. Although this diffusivity was determined for Mg-Fe interdiffusion in olivine, it was chosen here because there is no available data for Fe self-diffusion in olivine at low oxygen fugacity. Iron diffusion in olivine was modelled using the following relationship:

$$\frac{\partial C}{\partial t} = \frac{1}{r^2}\frac{\partial}{\partial r}\left(r^2 D \frac{\partial C}{\partial r}\right) \qquad \text{Eq. S-6}$$

where C is Fa#, t is time, r is radius and D is the temperature-dependent diffusion coefficient. Isotope profiles are calculated assuming $\beta = 0.16$ (Sio *et al*., 2018).

The timing and depth of olivine-metal mixing on the MGP parent body is unknown. We therefore performed chemical diffusion models for samples formed at depths between the base of the regolith and the core mantle boundary, in 2 km increments, and for olivine-metal mixing events that occurred at different times in the history of the planetesimal, from 1 Myr to the end of core crystallisation. Each diffusion model therefore utilised the thermal history for an olivine-metal assemblage that was formed at a unique time and depth in the parent body. The initial temperature of the core and mantle was 1600 K and the megaregolith was at 250 K. These parent-body parameters were chosen as they are compatible with the results of palaeomagnetic studies on MGP (Tarduno *et al*., 2012; Bryson *et al*., 2015). Figure 3a displays the results of one of these models, for a 200 km radius pallasite parent body, with the core-mantle boundary located at 100 km

depth, and the surface covered by an 8 km thick megaregolith. The black dashed equilibrium curve in Figure 3a marks the depth below which olivine-metal equilibration occurs. Note that dissolution-reprecipitation processes such as Ostwald ripening are not considered in our model but might accelerate the approach to isotopic equilibrium. Incorporating such effects would therefore move the black dashed curve shown in Figure 3 to shallower depths, further restricting the range of permissible conditions. Our displayed equilibrium curve should thus be considered a maximum depth for olivine-metal mixing.

Our results indicate that olivine-metal emplacement close to the core-mantle boundary will result in Fe isotope equilibration. This result persists for a wide range of plausible planetesimal radii, regolith thicknesses, and core/mantle mass ratios, thus precluding a core-mantle boundary origin for the MGP. Instead, our models imply olivine-metal mixing occurred in the shallow- to mid-mantle, in excellent agreement with the results of palaeomagnetic studies (Tarduno *et al.*, 2012; Bryson *et al.*, 2015). For comparison, we have indicated on Figure 3a the range of emplacement depths and period of cloudy zone formation determined for the Esquel and Imilac MGP, following the approach of Bryson *et al.* (2015). These depths lie well above the equilibration line determined for the same thermal model and are thus consistent with the observed Fe isotope disequilibrium in MGP.

Table S-2 Parameter values used for planetesimal thermal model.

Parameter	Description	Value	Unit
C_{pc}	Heat capacity of the core	850	J / kg / K
κ_r	Thermal diffusivity of the megaregolith	5E-8	m^2 / s
κ_m	Thermal diffusivity of the mantle	5E-7	m^2 / s
L_c	Specific latent heat of the core	270,000	J / kg
ρ_c	Density of the core	7,800	kg / m^3
δr	Radius grid spacing	1000	m
δt	Time step	3.15E10	s

Supplementary Tables

Table S-3. Summary of iron isotope analyses measured using Nu Plasma II and comparison to literature data.

	Source	Sample #	Extraction	δ^{56}Fe	2SE	δ^{57}Fe	2SE	#a
Imilac								
Metal	Smithsonian	USNM 383b	Microdrilled	-0.003	0.024	0.017	0.032	2
	Weyer et al. 2005			*0.147*	*0.036*			
Olivine	Smithsonian	USNM 383b	Microdrilled	-0.017	0.025	-0.020	0.025	2
	Weyer et al. 2005			*-0.019*	*0.035*			
Brenham								
Metal	Smithsonian	USNM 154b	Microdrilled	0.036	0.033	0.028	0.055	2
	Weyer et al. 2005			*0.067*	*0.003*			
Olivine	Smithsonian	USNM 154b	Microdrilled	-0.001	0.039	-0.001	0.039	1
	Weyer et al. 2005			*-0.007*	*0.010*			
Sulfide	Smithsonian		Microdrilled	-0.223	0.034	-0.391	0.125	1
Thiel Mtns.								
Metal	Smithsonian	USNM Z180i	Microdrilled	0.054	0.027	0.055	0.032	2
Olivine	Smithsonian	USNM Z180i	Microdrilled	0.011	0.085	0.011	0.085	1
Sulfide	Smithsonian	USNM Z180i	Microdrilled	-0.456	0.027	-0.629	0.090	2
Mt. Vernon								
Metal	Smithsonian	USNM 300d	Microdrilled	0.064	0.036	0.124	0.080	1
Olivine	Smithsonian	USNM 300d	Microdrilled	0.055	0.031	0.055	0.031	1
	Weyer et al. 2005			*0.043*	*0.013*			
Brahin								
Metal	Smithsonian	USNM 7018b	Microdrilled	0.072	0.041	0.112	0.112	1
	ROM	M50209	Hand-picked	0.259	0.049	0.455	0.128	1
Olivine (USN	Smithsonian	USNM 7018b	Microdrilled	0.051	0.060	0.051	0.060	1
	ROM	M50209	Hand-picked	0.001	0.034	0.037	0.082	2
	Weighted average			0.014	0.030	0.046	0.048	
	Weyer et al. 2005			*0.022*	*0.036*			
Springwater								
Metal	Smithsonian	USNM 868a	Microdrilled	0.065	0.023	0.092	0.030	2
	ROM	M56010	Hand-picked	-0.102	0.065	-0.100	0.098	1
	Poitrasson et al. 2005					*0.162*	*0.056*	
Olivine	Smithsonian	USNM 868a	Microdrilled	0.049	0.057	0.049	0.057	1
	ROM	M56010	Hand-picked	0.011	0.047	0.032	0.083	2
	Weighted average			0.026	0.036	0.044	0.047	
	Poitrasson et al. 2005					*0.021*	*0.085*	
Sulfide	Smithsonian	USNM 868a	Microdrilled	-0.445	0.050	-0.699	0.093	1
Giroux								
Metal	Smithsonian	USNM 1574b	Microdrilled	0.068	0.057	0.068	0.057	1
	ROM		Hand-picked	0.160	0.112	0.482	0.219	1
Olivine	Smithsonian	USNM 1574b	Microdrilled	-0.113	0.102	-0.024	0.131	1
	ROM (brown)		Hand-picked	-0.044	0.013	-0.045	0.048	
	Weighted average			-0.045	0.012	-0.043	0.045	

Table S-3 cont. Summary of iron isotope analyses measured using Nu Plasma II and comparison to literature data.

	Source	Sample #	Extraction	δ^{56}Fe	2SE	δ^{57}Fe	2SE	#a
Krasnojarsk								
Metal	Smithsonian	USNM 1057	Microdrilled	0.075	0.088	0.011	0.167	1
Olivine	Smithsonian	USNM 1057	Microdrilled	0.028	0.049	0.282	0.184	1
Fukang								
Metal	Purchased		Microdrilled	0.052	0.065	0.035	0.050	2
	ROM	M56846	Hand-picked	0.068	0.035	0.052	0.096	1
	Chernonozhkin et al. 2016			_0.247_	_0.018_	_0.332_	_0.032_	
Olivine	Purchased		Microdrilled	-0.004	0.110	-0.064	0.202	1
	Purchased		Hand-picked	-0.012	0.050	0.010	0.038	1
	ROM (brown)	M56846	Hand-picked	-0.004	0.099	-0.168	0.314	1
	Weighted average			-0.009	0.041	0.005	0.037	
	Chernonozhkin et al. 2016			_-0.075_	_0.015_	_-0.129_	_0.026_	
Esquel								
Metal	ROM	M47667	Microdrilled	0.072	0.043	0.086	0.062	2
	ROM	M47667	Hand-picked	0.185	0.272	0.455	0.624	1
	Poitrasson et al. 2005					_0.237_	_0.055_	
	Chernonozhkin et al. 2016			_0.095_	_0.026_			
Olivine	ROM	M47667	Microdrilled	-0.105	0.048	-0.117	0.155	2
	ROM	M47667	Hand-picked	-0.006	0.049	0.005	0.161	1
	Weighted average			_-0.057_	_0.034_	_-0.058_	_0.112_	
	Poitrasson et al. 2005					_-0.084_	_0.051_	
	Chernonozhkin et al. 2016			_-0.095_	_0.034_	_-0.127_	_0.023_	
Seymchan								
Metal	Purchased		Microdrilled	0.058	0.040	0.165	0.093	2
	Chernonozhkin et al. 2016			_0.023_	_0.013_	_-0.008_	_0.040_	
Olivine	Purchased		Microdrilled	-0.026	0.062	0.047	0.096	2
	Chernonozhkin et al. 2016			_-0.155_	_0.080_	_-0.192_	_0.028_	

#a indicates the number of analyses, each consisting of 5-9 replicates (i.e., n = 5-9) of 20 cycles with 4s integration time.

ROM (brown) notes that the olivine appeared brown in color compared to the Smithsonian samples.

All handpicked olivine data are used to give weighted average for olivine δ^{56}Fe compositions.

None of the handpicked metal values are used in calculating olivine-metal Fe isotope fractionations.

Literature data are for comparison purposes only.

Table S-4. Measured olivine-metal isotope fractionations in main-group pallasites.

	^{o}C/Myr	2SE	$\Delta^{56}Fe_{ol-met}$	2SE	$\Delta^{57}Fe_{ol-met}$	2SE
Esquel	3.0	0.7	-0.129	0.055	-0.081	0.128
Krasnojarsk	3.8	0.4	-0.046	0.101	0.271	0.248
Imilac	3.9	0.3	-0.014	0.035	-0.036	0.040
Springwater	5.0	0.3	-0.038	0.043	-0.048	0.056
Brahin	5.2	1.1	-0.058	0.050	-0.066	0.122
Fukang	5.3	1.4	-0.062	0.077	-0.030	0.062
Mt. Vernon	5.6	0.7	-0.009	0.047	-0.069	0.086
Brenham	6.1	0.5	-0.037	0.051	-0.029	0.068
Seymchan	6.2	0.8	-0.084	0.074	-0.118	0.133
Giroux	6.6	1.3	-0.113	0.058	-0.092	0.143
Thiel Mountains	-	-	-0.043	0.090	-0.044	0.091
Weighted average			**-0.049**	**0.016**	**-0.043**	**0.023**

Note: Cooling rates and error calculated based on cloudy zone particle sizes and Figure 8a of Yang *et al*. (2010).

Table S-5. Geostandard values processed with pallasite and experimental samples.

	$\delta^{56}Fe$	2SE	$\delta^{57}Fe$	2SE	n	Instrument
AGV	0.125	0.031	0.210	0.099	9	Nu Plasma II
Expected	*0.105*	*0.011*	*0.146*	*0.016*		
BCR	0.086	0.045	0.139	0.112	9	Nu Plasma II
Expected	*0.091*	*0.011*	*0.126*	*0.017*		
BHVO	0.113	0.049	0.208	0.082	9	Nu Plasma II
Expected	*0.114*	*0.011*	*0.174*	*0.016*		
BIR	0.061	0.044	0.120	0.100	9	Nu Plasma II
Expected	*0.053*	*0.015*	*0.087*	*0.023*		
PCC	0.025	0.020	0.067	0.035	6	Neptune Plus
Expected	*0.025*	*0.012*	*0.053*	*0.018*		
W2	0.063	0.038	0.053	0.097	9	Nu Plasma II
Expected	*0.056*	*0.013*	*0.076*	*0.020*		

Expected values are from Craddock and Dauphas (2011).
n indicates blocks each consisting of 20 cycles with 4s integration time.

Table S-6. Electron probe analyses of experimental run products; uncertainties are 1SD (n = 4 to 10).

		PaUCD7		PaUCD8		PaUCD10		PaUCD11	
Duration (hr)		3.5		23		95		72	
magnesiowustite	SiO$_2$	**0.09**	± 0.02	-	-	-	-	-	-
	MgO	**17.93**	± 0.63	**16.89**	± 0.38	**17.59**	± 0.76	**16.53**	± 3.81
	FeO	**82.01**	± 0.71	**82.26**	± 0.61	**81.03**	± 1.01	**81.83**	± 4.01
	NiO	**0.08**	± 0.11	**0.08**	± 0.12	**0.11**	± 0.12	**0.35**	± 0.26
	Total	**100.11**		**99.23**		**98.73**		**98.71**	
	$X_{Fe} / (X_{Fe} + X_{Mg})$	**0.72**	± 0.01	**0.73**	± 0.01	**0.72**	± 0.01	**0.74**	± 0.05
olivine	SiO$_2$	**38.49**	± 0.23	**38.09**	± 0.12	**38.15**	± 0.44	**38.52**	± 0.12
	MgO	**41.40**	± 0.45	**40.49**	± 0.12	**41.04**	± 0.48	**41.62**	± 0.11
	FeO	**21.70**	± 0.63	**22.73**	± 0.21	**21.80**	± 0.41	**20.97**	± 0.31
	NiO	**0.09**	± 0.12	**0.04**	± 0.06	**0.06**	± 0.07	**0.21**	± 0.12
	Total	**101.68**		**101.34**		**101.05**		**101.31**	
	$X_{Fe} / (X_{Fe} + X_{Mg})$	**0.23**	± 0.01	**0.24**	± 0.00	**0.23**	± 0.01	**0.22**	± 0.00
metal	Si	**0.01**	± 0.01	**0.00**	± 0.00	**0.01**	± 0.00	**0.00**	± 0.00
	[a]C	**4.69**	± 1.28	**4.96**	± 0.78	**4.68**	± 0.31	**4.33**	± 0.23
	Fe	**96.25**	± 1.20	**95.93**	± 0.81	**96.47**	± 0.58	**84.61**	± 0.50
	Ni	**0.07**	± 0.06	**0.06**	± 0.05	**0.05**	± 0.10	**11.81**	± 0.36
	Total	**101.02**		**100.96**		**101.21**		**100.75**	
	[b]ΔIW	0.12		0.17		0.12		0.22	

[a]Carbon value following blank subtraction made using the pure Fe NIST2168 standard (n = 10)

[b]Oxygen fugacity calculated relative to the iron-wustite buffer using $\Delta IW = 2\log(a_{FeO}(mw) / a_{Fe}(met))$. Activity coefficients for Fe in the metal calculated using the method of Ma (2001) and interaction parameters for carbon saturated systems from the Steelmaking Data Sourcebook. FeO in the mw phase is assumed to be ideal.

Table S-7. Olivine-metal isotope fractionation in time series experiment, corrected for metal contamination in "olivine" fractions.

	Duration (hr)	Metal	Uncorrected $\Delta^{56}Fe_{ol\text{-}met}$	Uncorrected $\Delta^{57}Fe_{ol\text{-}met}$	Corrected $\Delta^{56}Fe_{ol\text{-}met}$	Corrected $\Delta^{57}Fe_{ol\text{-}met}$
PaUCD7	3.5	Fe$_{82}$C$_{18}$	0.350 ± 0.097	0.339 ± 0.165	0.372 $^{-\ 0.119}_{+\ 0.132}$	0.360 $^{-\ 0.187}_{+\ 0.209}$
PaUCD8	23	Fe$_{81}$C$_{19}$	0.115 ± 0.043	0.132 ± 0.083	0.115 $^{-\ 0.043}_{+\ 0.047}$	0.132 $^{-\ 0.083}_{+\ 0.089}$
PaUCD9	48	*Fe$_{82}$C$_{18}$	0.048 ± 0.023	0.063 ± 0.045	0.059 $^{-\ 0.030}_{+\ 0.034}$	0.078 $^{-\ 0.057}_{+\ 0.064}$
PaUCD10	95	Fe$_{82}$C$_{18}$	0.021 ± 0.033	0.032 ± 0.032	0.059 $^{-\ 0.093}_{+\ 0.107}$	0.091 $^{-\ 0.091}_{+\ 0.105}$
PaUCD11	72	Fe$_{73}$Ni$_{10}$C$_{17}$	0.024 ± 0.024	0.063 ± 0.020	0.042 $^{-\ 0.043}_{+\ 0.050}$	0.114 $^{-\ 0.046}_{+\ 0.047}$

All measured using Neptune Plus. Metal was used as the bracketing standard for the corresponding "olivine" fractions.

*The metal composition for PaUCD9 was not measured, but expected to be the same as PaUCD10.

Corrected Δ-values made based on EMPA data and ICPMS Fe/Mg ratios measured on the dissolved olivine+magnesiowustite fractions.

Uncertainties of the corrected Δ-values include uncertainty in level of metal contamination and refer to the lowest and highest values possible.

Corrected Δ-values are plotted in all figures.

Supplementary Information References

Belashchenko, D. K., Mirzoev, A., Ostrovski, O. (2011) Molecular dynamics modelling of liquid Fe-C alloys. *High Temperature Materials and Processes* 30, 297–303. https://doi.org/10.1515/htmp.2011.048

Blanchard, M., Poitrasson, F., Meheut, M., Lazzeri, M., Mauri, F., Balan, E. (2009) Iron isotope fractionation between pyrite (FeS_2), hematite (Fe_2O_3) and siderite ($FeCO_3$): a first-principles density functional theory study. *Geochimica et Cosmochimica Acta* 73, 6565–6578. https://doi.org/10.1016/j.gca.2009.07.034

Bourdon, B., Roskosz, M., Hin, R.C. (2018) Isotope tracers of core formation. *Earth-Science Reviews* 181, 61–81. https://doi.org/10.1016/j.earscirev.2018.04.006

Brockhouse, B.N., Abou-Helal, H.E., Hallman, E.D. (1967) Lattice vibrations in iron at 296 K. *Solid State Communications* 5, 211–216. https://doi.org/10.1016/0038-1098(67)90258-X

Bryson, J.F., Nichols, C.I., Herrero-Albillos, J., Kronast, F., Kasama, T., Alimadadi, H., van der Laan, G. Nimmo, F., Harrison, R.J. (2015) Long-lived magnetism from solidification-driven convection on the pallasite parent body. *Nature* 517, 472–475. https://doi.org/10.1038/nature14114

Buseck, P.R. (1977) Pallasite meteorites—mineralogy, petrology and geochemistry. *Geochimica et Cosmochimica Acta* 41, 711–740. https://doi.org/10.1016/0016-7037(77)90044-8

Chernonozhkin, S.M., Goderis, S., Costas-Rodríguez, M., Claeys, P., Vanhaecke, F. (2016) Effect of parent body evolution on equilibrium and kinetic isotope fractionation: a combined Ni and Fe isotope study of iron and stony-iron meteorites. *Geochimica et Cosmochimica Acta*, *186*, 168–188. https://doi.org/10.1016/j.gca.2016.04.050

Chernonozhkin, S.M., Weyrauch, M., Goderis, S., Oeser, M., McKibbin, S.J., Horn, I., Hecht, L., Weyer, S., Claeys, P., Vanhaecke, F. (2017) Thermal equilibration of iron meteorite and pallasite parent bodies recorded at the mineral scale by Fe and Ni isotope systematics. *Geochimica et Cosmochimica Acta* 217, 95–111. https://doi.org/10.1016/j.gca.2017.08.022

Condit, R.H., Hobbins, R.R., Birchenall, C.E. (1974) Self-diffusion of iron and sulfur in ferrous sulfide. *Oxidation of metals* 8, 409–455. https://doi.org/10.1007/BF00603390

Craddock, P.R., Dauphas, N. (2011) Iron isotopic compositions of geological reference materials and chondrites. *Geostandards and Geoanalytical Research* 35, 101–123. https://doi.org/10.1111/j.1751-908X.2010.00085.x

Dal Corso, A. (2014) Pseudopotentials periodic table: From H to Pu. *Computational Materials Science* 95, 337-350. https://doi.org/10.1016/j.commatsci.2014.07.043

Dauphas, N. (2007) Diffusion-driven kinetic isotope effect of Fe and Ni during formation of the Widmanstätten pattern. *Meteoritics & Planetary Science* 42, 1597–1613. https://doi.org/10.1111/j.1945-5100.2007.tb00593.x

Dauphas, N., Roskosz, M., Alp, E.E., Golden, D.C., Sio, C.K., Tissot, F.L. H., Hu, M.Y., Zhao, J., Gao, L., Morris, R. V. (2012) A general moment NRIXS approach to the determination of equilibrium Fe isotopic fractionation factors: application to goethite and jarosite. *Geochimica et Cosmochimica Acta* 94, 254–275. https://doi.org/10.1016/j.gca.2012.06.013

Dauphas, N., Roskosz, M., Alp, E.E., Neuville, D.R., Hu, M.Y., Sio, C.K., Tissot, F.L.H., Zhao, J., Tissandier, L., Médard, E., Cordier, C. (2014) Magma redox and structural controls on iron isotope variations in Earth's mantle and crust. *Earth and Planetary Science Letters* 398, 127–140. https://doi.org/10.1016/j.epsl.2014.04.033

Dodson, M.H. (1973) Closure temperature in cooling geochronological and petrological systems. *Contributions to Mineralogy and Petrology* 40, 259–274. https://doi.org/10.1007/BF00373790

Dohmen, R., Chakraborty, S. (2007) Fe–Mg diffusion in olivine II: point defect chemistry, change of diffusion mechanisms and a model for calculation of diffusion coefficients in natural olivine. *Physics and Chemistry of Minerals* 34, 409–430; and its erratum. https://doi.org/10.1007/s00269-007-0158-6

Elardo, S.M., Shahar, A. (2017) Non-chondritic iron isotope ratios in planetary mantles as a result of core formation. *Nature Geoscience* 10, 317–321. https://doi.org/10.1038/ngeo2896

Elcombe M.M., Hulston J.R. Calculation of sulphur isotope fractionation between sphalerite and galena using lattice dynamics (1975) *Earth and Planetary Science Letters* 28, 172–180. https://doi.org/10.1016/0012-821X(75)90224-1

Garrity, K.F., Bennett, J.W., Rabe, K.M., Vanderbilt, D. (2014) Pseudopotentials for high-throughput DFT calculations. *Computational Materials Science* 81, 446–452. https://doi.org/10.1016/j.commatsci.2013.08.053

Giannozzi, P., Baroni, S., Bonini, N., Calandra, M., Car, R., Cavazzoni, C., Ceresoli, D., Chiarotti, G.L., Cococcioni, M., Dabo, I., Dal Corso, A., Fabris, S., Fratesi, G., de Gironcoli, S., Gebauer, R., Gerstmann, U., Gougoussis, C., Kokalj, A., Lazzeri, M., Martin-Samos, L., Marzari, N., Mauri, F., Mazzarello, R., Paolini, S., Pasquarello, A., Paulatto, L., Sbraccia, C., Scandolo, S., Sclauzero, G., Seitsonen, AP., Smogunov, A., Umari, P., Wentzcovitch, R.M. (2009) QUANTUM ESPRESSO: a modular and open-source software project for quantum simulations of materials. *Journal of Physics: Condensed Matter* 21, 395502. https://doi.org/10.1088/0953-8984/21/39/395502

Guignard, J., Bystricky, M., Toplis, M.J. (2012) Grain growth in forsterite–nickel mixtures: analogues of small parent bodies during early accretion. *Physics of the Earth and Planetary Interiors* 204, 37–51. https://doi.org/10.1016/j.pepi.2012.06.002

Heinemann R., Kroll H., Kirfel A., Barbier B. (2007) Order and anti-order in olivine III: Variation of the cation distribution in the Fe,Mg olivine solid solution series with temperature and composition. *European Journal of Mineralogy* 19, 15–27. https://doi.org/10.1127/0935-1221/2007/0019-0015

Liu, J., Dauphas, N., Roskosz, M., Hu, M.Y., Yang, H., Bi, W., Zhao, J., Alp, E.E., Hu, J.Y., Lin, J.F. (2017) Iron isotopic fractionation between silicate mantle and metallic core at high pressure. *Nature Communications* 8, 1–6. https://doi.org/10.1038/ncomms14377

Ma, Z. (2001) Thermodynamic description for concentrated metallic solutions using interaction parameters. *Metallurgical and Materials Transactions B* 32, 87–103. https://doi.org/10.1007/s11663-001-0011-0

Matsuhisa, Y., Goldsmith, J.R., Clayton, R.N. (1978) Mechanisms of hydrothermal crystallization of quartz at 250 °C and 15 kbar. *Geochimica et Cosmochimica Acta* 42, 173–182. https://doi.org/10.1016/0016-7037(78)90130-8

Nafziger, R.H., Muan, A. (1967) Equilibrium phase compositions and thermodynamic properties of olivines and pyroxenes in the system MgO–"FeO"–SiO$_2$. *American Mineralogist* 52, 1364-1385.

Nie, N.X., Dauphas, N., Alp, E.E., Zeng, H., Sio, C.K., Hu, J.Y., Chen, X., Aarons, S.M., Zhang, Z., Tian, H.-C., Wang, D., Prissel, K.B., Greer, J., Bi, W., Hu, M.Y., Zhao, J., Shahar, A., Roskosz, M., Teng, F.-Z., Krawczynski, M.J., Heck, P.R., Spear, F.S. (2021) Iron, magnesium, and titanium isotopic fractionations between garnet, ilmenite, fayalite, biotite, and tourmaline: Results from NRIXS, ab initio, and study of mineral separates from the Moosilauke metapelite. *Geochimica et Cosmochimica Acta* 302, 18–45. https://doi.org/10.1016/j.gca.2021.03.014

Perdew, J.P., Burke, K., Ernzerhof, M. (1996) Generalized gradient approximation made simple. *Physical Review Letters* 77, 3865–3868. https://doi.org/10.1103/PhysRevLett.77.3865

Poitrasson, F., Levasseur, S., Teutsch, N. (2005) Significance of iron isotope mineral fractionation in pallasites and iron meteorites for the core–mantle differentiation of terrestrial planets. *Earth and Planetary Science Letters* 234, 151–164. https://doi.org/10.1016/j.epsl.2005.02.010

Poitrasson, F., Roskosz, M., Corgne, A. (2009) No iron isotope fractionation between molten alloys and silicate melt to 2000 C and 7.7 GPa: Experimental evidence and implications for planetary differentiation and accretion. *Earth and Planetary Science Letters* 278, 376–385. https://doi.org/10.1016/j.epsl.2008.12.025

Roskosz, M., Sio, C.K., Dauphas, N., Bi, W., Tissot, F.L., Hu, M.Y., Zhao, J., Alp, E.E. (2015) Spinel–olivine–pyroxene equilibrium iron isotopic fractionation and applications to natural peridotites. *Geochimica et Cosmochimica Acta* 169, 184–199. https://doi.org/10.1016/j.gca.2015.07.035

Saiki, K., Laporte, D., Vielzeuf, D., Nakashima, S., Boivin, P. (2003) Morphological analysis of olivine grains annealed in an iron-nickel matrix: Experimental constraints on the origin of pallasites and on the thermal history of their parent bodies. *Meteoritics & Planetary Science* 38, 427–444. https://doi.org/10.1111/j.1945-5100.2003.tb00278.x

Schauble, E.A. (2011) First-principles estimates of equilibrium magnesium isotope fractionation in silicate, oxide, carbonate and hexaaquamagnesium(2+) crystals. *Geochimica et Cosmochimica Acta* 75, 844–869. https://doi.org/10.1016/j.gca.2010.09.044

Shahar, A., Young, E.D., Manning, C.E. (2008) Equilibrium high-temperature Fe isotope fractionation between fayalite and magnetite: an experimental calibration. *Earth and Planetary Science Letters* 268, 330–338. https://doi.org/10.1016/j.epsl.2008.01.026

Shahar, A., Schauble, E.A., Caracas, R., Gleason, A.E., Reagan, M.M., Xiao, Y., Shu, J., Mao, W. (2016) Pressure-dependent isotopic composition of iron alloys. *Science* 352, 580–582. https://doi.org/10.1126/science.aad9945

Shibazaki, Y., Kono, Y., Fei, Y. (2015) Microscopic structural change in a liquid Fe-C alloy of~ 5 GPa. *Geophysical Research Letters* 42, 5236–5242. https://doi.org/10.1002/2015GL064271

Smith, E.M., Ni, P., Shirey, S.B., Richardson, S. H., Wang, W., Shahar, A. (2021) Heavy iron in large gem diamonds traces deep subduction of serpentinized ocean floor. *Science Advances* 7, eabe9773. https://doi.org/10.1126/sciadv.abe9773

Sio, C.K., Roskosz, M., Dauphas, N., Bennett, N.R., Mock, T., Shahar, A. (2018) The isotope effect for Mg-Fe interdiffusion in olivine and its dependence on crystal orientation, composition and temperature. *Geochimica et Cosmochimica Acta* 239, 463–480. https://doi.org/10.1016/j.gca.2018.06.024

Solferino, G.F., Golabek, G.J., Nimmo, F., Schmidt, M.W. (2015) Fast grain growth of olivine in liquid Fe–S and the formation of pallasites with rounded olivine grains. *Geochimica et Cosmochimica Acta* 162, 259–275. https://doi.org/10.1016/j.gca.2015.04.020

Sossi, P.A., O'Neill, H.S.C. (2017) The effect of bonding environment on iron isotope fractionation between minerals at high temperature. *Geochimica et Cosmochimica Acta* 196, 121–143. https://doi.org/10.1016/j.gca.2016.09.017

Steelmaking Data Sourcebook (1988) The Japan Society for the Promotion of Science: The 19th Committee on Steelmaking. Gordon and Breach Science Publishers, New York.

Tarduno, J.A., Cottrell, R.D., Nimmo, F., Hopkins, J., Voronov, J., Erickson, A., Blackman, E., Scott, E.R.D., McKinley, R. (2012) Evidence for a dynamo in the main group pallasite parent body. *Science* 338, 939–942. https://doi.org/10.1126/science.1223932

Trail, D., Savage, P.S., Moynier, F. (2019) Experimentally determined Si isotope fractionation between zircon and quartz. *Geochimica et Cosmochimica Acta* 260, 257–274. https://doi.org/10.1016/j.gca.2019.06.035

Waseda, Y., Ohtani, M. (1974) Static structure of liquid noble and transition metals by X-ray diffraction. *Physica Status Solidi (B)* 62, 535–546. https://doi.org/10.1002/pssb.2220620224

Wasson, J.T., Choi, B.G. (2003) Main-group pallasites: Chemical composition, relationship to IIIAB irons, and origin. *Geochimica et Cosmochimica Acta* 67, 3079–3096. https://doi.org/10.1016/S0016-7037(03)00306-5

Weyer, S., Anbar, A.D., Brey, G.P., Münker, C., Mezger, K., Woodland, A.B. (2005) Iron isotope fractionation during planetary differentiation. *Earth and Planetary Science Letters* 240, 251–264. https://doi.org/10.1016/j.epsl.2005.09.023

Widanagamage, I.H., Schauble, E.A., Scher, H.D., Griffith, E.M. (2014) Stable strontium isotope fractionation in synthetic barite. *Geochimica et Cosmochimica Acta* 147, 58–75. https://doi.org/10.1016/j.gca.2014.10.004

Wiser, N.M., Wood, B.J. (1991) Experimental determination of activities in Fe–Mg olivine at 1400 K. *Contributions to Mineralogy and Petrology* 108, 146-153. https://doi.org/10.1007/BF00307333

Yang, C.W., Williams, D.B., Goldstein, J.I. (1996) A revision of the Fe-Ni phase diagram at low temperatures (< 400 C). *Journal of Phase Equilibria* 17, 522–531. https://doi.org/10.1007/BF02665999

Yang, J., Goldstein, J.I., Scott, E.R. (2010) Main-group pallasites: thermal history, relationship to IIIAB irons, and origin. *Geochimica et Cosmochimica Acta* 74, 4471–4492. https://doi.org/10.1016/j.gca.2010.04.016